

Modeling ground motions and crustal deformation from tsunami earthquakes: Rupture parameter constraints from the 2010 Mentawai event

Tara A. Nye  * ^{† 1}, Valerie J. Sahakian  ¹, Diego Melgar  ¹

¹Department of Earth Sciences, University of Oregon, Eugene, Oregon, USA

Author contributions: *Conceptualization:* Tara A. Nye, Valerie J. Sahakian, Diego Melgar. *Methodology:* people. *Formal Analysis:* Tara A. Nye, Valerie J. Sahakian, Diego Melgar. *Investigation:* Tara A. Nye. *Writing - Original draft:* Tara A. Nye. *Writing - Review & Editing:* Tara A. Nye, Valerie J. Sahakian, Diego Melgar. *Visualization:* Tara A. Nye. *Supervision:* Valerie J. Sahakian, Diego Melgar. *Project administration:* Valerie J. Sahakian. *Funding acquisition:* Valerie J. Sahakian, Diego Melgar.

Abstract We use a combination of near-field simulated and observational data to constrain the rise time, rupture velocity, and high-frequency stress parameter for the 2010 M_w 7.8 Mentawai tsunami earthquake. Tsunami earthquakes, which are shallow-rupturing events that generate exceptionally large seafloor displacements, are challenging for current tsunami early warning systems. A combination of near-field high-rate GNSS and seismic data can be used for early discrimination, but the dearth of data from these events limits testing of such an implementation in a real-time scenario. In lieu of near-field data, models with realistic rupture physics can be leveraged to improve local tsunami warning. We develop recommendations for such parameters based on observations of near-field data from the 2010 M_w 7.8 Mentawai earthquake. We find that the rise time and rupture velocity covary, and that rise time–rupture velocity combinations ranging from 5.4 s–1.26 km/s to 12.0 s–1.60 km/s adequately model the long duration of the Mentawai event. We find that a stress parameter of 1.2 MPa best models the high-frequency deficiency. We present equations which can be used to determine reasonable parameter values for simulating tsunami earthquakes, and we find that simulated data generated with the recommended parameters capture defining characteristics of tsunami earthquakes.

Non-technical summary Tsunami earthquakes are events that have a moderate moment magnitude, produce weak shaking in the near-field, yet generate exceptionally large tsunamis. The impending hazard from these events is generally underestimated by tsunami early warning systems, which rely primarily on the earthquake magnitude. A recent study suggests a joint analysis of near-field high-rate GNSS and seismic data can be used to identify these destructive events and provide adequate warning times. Because these earthquakes are rare, little data exist to test this algorithm. Thus, we evaluate which parameters and their values are needed to simulate tsunami earthquakes as a supplement for real tsunami earthquake data. We simulate earthquake scenarios patterned after the 2010 Mentawai tsunami earthquake, the only tsunami earthquake recorded in the near-field, and determine which combinations of parameters best recreate the real Mentawai data. We also present two equations that can be used to select rupture parameter values to simulate tsunami earthquake-type events.

Production Editor:
Gareth Funning
Handling Editor:
Mathilde Radiguet
Copy & Layout Editor:
Anna Ledeczi

Received:
17 November 2023
Accepted:
4 September 2024
Published:
27 September 2024

1 Introduction

Tsunami earthquakes are rare, end-member earthquakes that generate tsunamis much larger in height than expected for their magnitude (Kanamori, 1972). These are around a moment magnitude (M_w) 7–8, but the runup is on the order of $10\times$ greater than that of a typical megathrust earthquake of similar magnitude (Hill et al., 2012; Sahakian et al., 2019; Satake et al., 1993). This tsunami amplification, or *tsunami efficiency* (Kajiura, 1970; Lotto et al., 2017; Miyoshi, 1954; Riquelme and Fuentes, 2021), is a result of the shallow rupture of tsunami earthquakes (hereafter referred to as TsEs). TsEs rupture the updip region of the subducting slab (i.e., Domain A; Lay et al., 2012), a region

generally considered aseismic due to the low confining pressures and high pore fluid pressures. These conditions yield velocity-strengthening frictional properties, which result in predominantly stable sliding and do not allow for elastic strain accumulation (Lay and Bilek, 2007; Lay et al., 2012). On occasion, shallow megathrust slip is observed, such as when shallow slow slip events are recorded, or when the shallow megathrust ruptures seismically as a TsE.

TsEs pose a significant threat to affected regions, not only because the tsunamis are unexpectedly large, but also because the shaking is milder than expected compared to their moment magnitude. TsEs are depleted in high frequencies due to the slower rupture velocity (V_{rupt}) (Yao et al., 2013), which means compared to a typical earthquake of the same magnitude, a TsE would produce unexpectedly low shaking in the near-field (Sa-

*Corresponding author: tnye@usgs.gov

[†]Now at the US Geological Survey, Moffett Field, California, USA

hakian et al., 2019; Wirth et al., 2022), and it would appear even smaller in magnitude when looking strictly at strong-motion data. Simply put, a TsE shakes like a M_w 6 but produces a tsunami like a M_w 9. Magnitude-driven tsunami early warning algorithms would thus underestimate the tsunami hazard, and in some regions where residents are encouraged to immediately seek higher ground if strong shaking is felt, the low shaking of a TsE would not necessarily suggest an impending large tsunami hazard. As such, many fatalities are common with tsunami earthquakes.

Early discrimination of these events is critical to provide ample warning to people within the inundation zone and reduce the number of casualties. Sahakian et al. (2019) suggest this may be possible using a combination of near-field high-rate Global Navigation Satellite Systems (HR-GNSS) and seismic data, which can indicate an energy-deficient event. Data are needed to test this in an early warning framework, but as near-field geophysical data currently only exist for the 2010 Mentawai TsE, simulated TsE data would be a valuable supplement (e.g., Lin et al., 2021; Tsushima and Ohta, 2014; Williamson et al., 2020). It is first necessary, however, to establish both the model parameters that control the behavior of TsEs and their expected values. We determine these key TsE rupture parameters and obtain their expected distributions by evaluating which combinations of parameters best recreate the observed near-field ground motions of the 2010 Mentawai event.

2 Background

TsEs are poorly understood, not only because of their infrequent occurrence and rupture outside of the typically seismic domain, but also because they do not appear to be biased towards any set of interface conditions. This makes assigning likelihoods to their future occurrence, locales, and other characteristics challenging. To date, we only have record of ~14 TsEs (some historical TsE classifications are debated) (Figure 1). Of these, eight occurred along erosional margins, and five occurred along accretionary margins with defined accretionary prisms, but this erosional margin bias is likely due to the greater percentage of erosional margins (~75%) globally (Lotto et al., 2017). These events have also occurred in settings with diverse plate bathymetry, varying convergence rate and obliquity, and varying plate age (Bilek and Lay, 2002; Geersen, 2019). Some studies suggest that TsEs favor regions with a morphologically complex subducting plate and insufficient trench sediments to level out the topography (Geersen, 2019); although, the 1907 Sumatra event is an exception. This may be especially true in regions with active shallow slow-slip events (Meng and Duan, 2022). The only seeming universality among all TsEs, however, appears to be their shallow rupture, which results in both slower and enhanced slip, regardless of the tectonic setting

In accretionary settings, a compliant prism of accreted sediment accumulates, and the low rigidity and inelastic deformation of the prism can enhance seafloor uplift and tsunami excitation (Bilek and Lay, 1999; Du

et al., 2021; Ma and Nie, 2019). Large-volume prisms increase tsunami height and tsunami efficiency by increasing the rate-and-state parameter ($b - a$) (Lotto et al., 2017), which renders the material more velocity-weakening and unstable (Dieterich, 1979; Ruina, 1983; Scholz, 1998). For example, the largest tsunami waves for the great 2011 M_w 9.0 Tohoku-Oki earthquake were observed ~100 km north of where the greatest slip occurred due to the greater presence of wedge sediments (Ma and Nie, 2019). Tsunami height is particularly correlated with the width and slope steepness of the outer wedge of the prism, depth of décollement beneath the seafloor, and presence of high-angle splay faults (Felix et al., 2021; Qiu and Barbot, 2022). The lower rigidity of the prism also decreases the shear wave velocity (V_s), which in turn is believed to lead to a slower V_{rupt} and subsequently longer rupture duration of the fault segment (Lay et al., 2011; Newman et al., 2011).

In erosional settings, sediment erodes the upper plate near the trench, and the downgoing plate develops a horst and graben structure which traps sediments (Geersen, 2019; Ruff, 1989). Although lacking a defined prism, the presence of some sediment in erosional margins still alters the frictional properties and can locally increase pore fluid pressure, resulting in greater but slow and jerky slip (Geersen, 2019; Lay and Bilek, 2007; Lotto et al., 2017; Kanamori and Kikuchi, 1993; Tanioka et al., 1997; Weinstein and Okal, 2005). The absence of a prism also allows for the potential to break the ocean floor and efficiently generate tsunamis (Kanamori and Kikuchi, 1993). Tsunamis generated by TsEs in these tectonic settings tend to be smaller in scale due to the smaller size (or lack thereof) of the outer wedge (Qiu and Barbot, 2022).

It is still unclear how the shallow aseismic domain hosts seismic events, but several theories have been proposed. Some studies suggest TsEs are generated by rupture of large asperities in conditionally stable regions just downdip of the aseismic zone, which then propagates into the aseismic domain if large enough (e.g., Bilek and Lay, 2002; Lay and Bilek, 2007; Lay et al., 2012). The 2011 Tohoku-Oki earthquake, although not a TsE, exemplifies this with its significant slip that ruptured through the shallow megathrust, possibly breaking the ocean floor (Jeppson et al., 2018). Although it seems any subduction zone could host a TsE (Bilek and Lay, 2002), the historical record is too short to conclude this. Shallow aftershocks of a 2007 Mentawai, traditionally-rupturing (i.e., not TsE), event suggest frictionally unstable patches are in fact present all the way to the trench (Collings et al., 2012). Hill et al. (2012) suggest that the rupture does not break the seafloor, but instead occurs along a blind thrust fault propagating along the base of the prism and extending to about 1.5 km below the surface. Because steeply dipping faults produce higher seafloor uplift, they could be a mechanism for TsEs (Kanamori and Kikuchi, 1993; Qiu and Barbot, 2022); the 1975 M_s 7.0 Kurile event is an example of this (Fukao, 1979). Although the mechanisms for seismicity along the shallow megathrust are debated, coseismic rupture is still possible along décollements (such as in the accretionary prism) regardless of tectonic setting,

plate age, or fault type (Hubbard et al., 2015). Despite the range of conditions and environments which have hosted TsEs, their resulting ground-motion data exhibit the same characteristics: long moment-rate-function and decreased high-frequency content.

Parameters relating radiated energy to seismic moment or duration are an effective discrimination tool as tsunami earthquakes radiate energy inefficiently and have longer durations compared to their moment (e.g., Newman et al., 2011; Newman and Okal, 1998; Weinstein and Okal, 2005). Such methods use teleseismic data and do not stabilize quickly enough to detect the TsE before inundation for near shore ruptures. The long duration of TsEs can also result in anomalous centroid time-delays, but such anomalies are not necessarily distinguishable from other anomalous events (Duputel et al., 2013).

Sahakian et al. (2019) proposed a discrimination method utilizing a combination of near-field HR-GNSS and seismic data, which can be calculated in near-real-time. Peak ground displacement (PGD) from HR-GNSS recordings is representative of the overall magnitude of the earthquake and is relatively insensitive to the shallow rupture processes. Conversely, peak ground acceleration (PGA) from seismic recordings is more sensitive to slow rupture of the shallow megathrust and reflects the energy deficiency of TsEs. This relationship can thus act as a proxy energy-to-moment parameter.

To support the testing and validation of such an algorithm in local tsunami warning, we establish model parameters needed to simulate tsunami earthquake-type events. We explore the rise time, V_{rupt} , and high-frequency stress parameter, which are known to be influenced by shallow megathrust properties and have been observed as characteristically different for TsEs (Lay et al., 2012; Melgar and Hayes, 2017; Riquelme et al., 2020; Riquelme and Fuentes, 2021; Ye et al., 2016). The rise time is the amount of time it takes for slip to initiate on a patch of the fault and for the healing front to move through. The weak zone of accreted sediments in the shallow megathrust lends to slower rise times (Graves and Pitarka, 2010; Melgar and Hayes, 2017). Melgar and Hayes (2017) include a figure of M_0 versus mean rise time for a synthesized database of recordings from $>150 M_w$ 7–9 events, four of which are TsEs (1994 and 2006 Java; 1994 Nicaragua; 2010 Mentawai) with mean rise times ranging from ~ 8 –20 s compared to ~ 2 –8 s for typical interplate events. V_{rupt} for standard earthquakes is typically around 1.5–2.5 km/s, but TsEs have shown to have a slower V_{rupt} ranging from 1–2 km/s (Riquelme et al., 2020) because of the low rigidity of the upper plate and frictional properties in a conditionally stable region (Bilek et al., 2011; Meng and Duan, 2023; Sallarès and Ranero, 2019; Sallarès et al., 2021). Lastly, as TsEs are biased towards low-frequency energy, their recordings tend to have lower corner frequencies, which are proportional to the stress parameter. The stress parameter is a difficult value to constrain, and values span orders of magnitude. However, an acceptable range for typical interface events is 3–12 MPa (Atkinson and Macias, 2009), whereas TsEs often have stress parameters less than 1 MPa (Bilek

et al., 2016; Ide et al., 1993; Kikuchi and Kanamori, 1995; Yue et al., 2014). Although previous studies have constrained values of these parameters for several tsunami earthquakes, it is unclear whether their prescription in a simplified model would necessarily generate data with the expected characteristics of TsEs, as the physics governing these models are informed by more typical events. With this study, we determine parameter values needed to simulate TsEs.

3 Data and Methods

3.1 Geophysical dataset

3.1.1 Observed data

The 2010 Mentawai TsE was recorded in the near-field on 13 HR-GNSS stations operated by Earth Observatory of Singapore, Nanyang Technological University (EOS-NTUS) and 17 strong-motion seismic stations operated by the Agency for Meteorology, Climatology, and Geophysics of Indonesia (BMKG). The number of stations is moderate; however, they have good azimuthal land coverage, and the number of stations is comparable to other megathrust event recordings (Sahakian et al., 2019). Both the seismic and HR-GNSS data come from the Ruhl et al. (2019) database. For this study, we eliminated eight seismic stations that had epicentral distances > 600 km to avoid surface wave bias of PGA, as well as eight HR-GNSS stations due to high noise levels. Our final dataset is shown in (Figure 2).

3.1.2 Simulated data

We use a set of semistochastic forward modeling codes, referred to as *FakeQuakes* (from the MudPy GitHub repository), to generate our simulation dataset (Melgar et al., 2016). *FakeQuakes* uses a one-dimensional (1D) velocity model to generate stochastic kinematic rupture models patterned after the 2010 Mentawai event, as well as the associated HR-GNSS and seismic waveforms. We use the Yue et al. (2014) velocity model for this study; however, we add additional columns for P and S wave intrinsic attenuation (Q_P and Q_S , respectively). Q is not well resolved in this region, so we constructed a crude 1D attenuation model using relationships between V_P and Q_P for the Hikurangi subduction zone (Eberhart-Phillips and Bannister, 2015; Eberhart-Phillips et al., 2014) and V_P for this region. Q_S was approximated as $0.5*Q_P$. A detailed explanation of the simulation methodology is provided in the following paragraphs.

Various slip inversion models exist for the 2010 Mentawai TsE, but as inversions are non-unique, we have generated a suite of 30 stochastic rupture models using a modified version of the Yue et al. (2014) slip inversion as a mean slip model. *FakeQuakes* allows one to generate rupture models that are perturbations of a background mean model. In this case, the mean model is a log-frequency derived slip inversion. This is a special characteristic of *FakeQuakes* compared to other stochastic rupture modeling codes (e.g., Graves and Pitarka, 2010, 2015; LeVeque et al., 2016) that was first introduced by Goldberg and Melgar (2020)

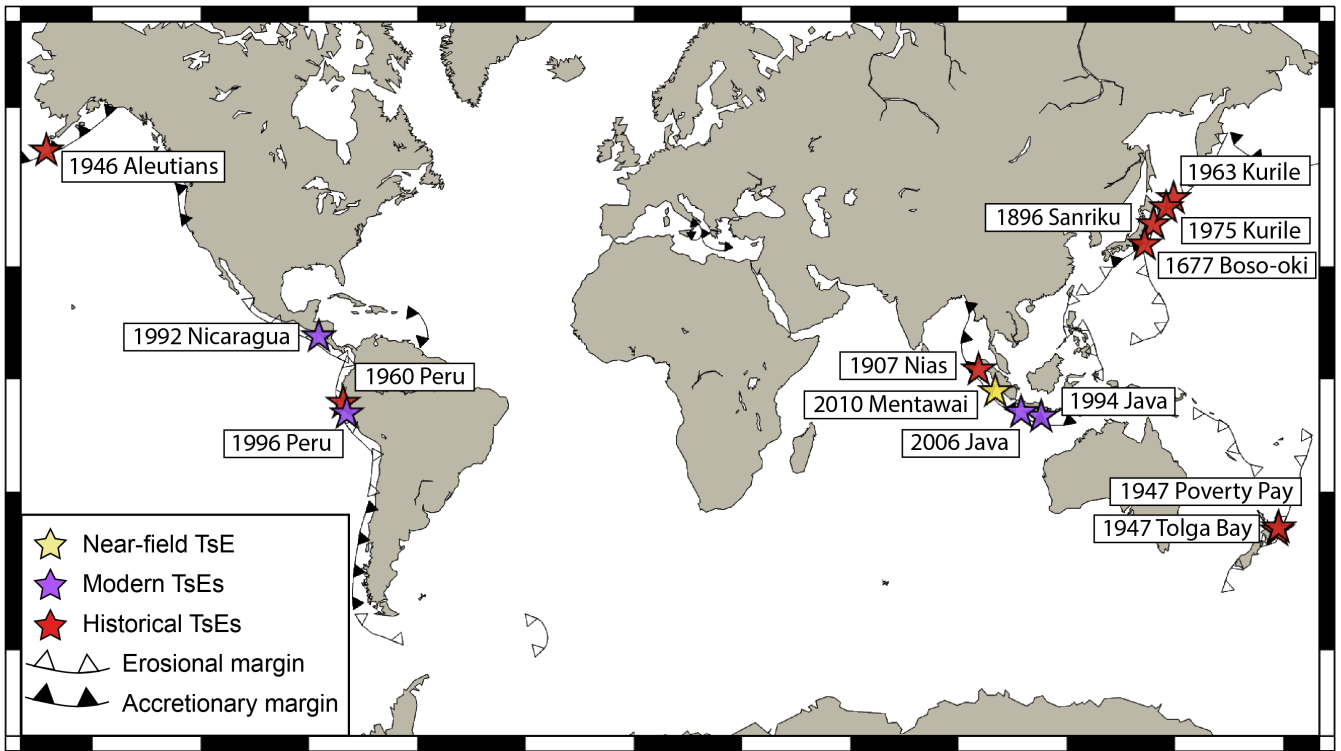


Figure 1 Global map of tsunami earthquakes (TsEs). Red stars and purple stars indicate TsEs that occurred before and after the widespread development of modern digital broadband seismic networks around the 1990s, and the yellow star indicates the only near-field recorded TsE to date. Subduction classifications are taken from Clift and Vannucchi (2004), where erosional margins are indicated by trench lines with open triangles, and accretionary margins are indicated by trench lines with filled triangles.

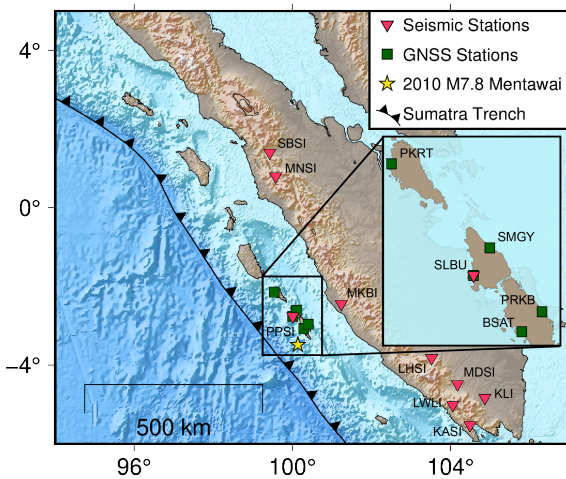


Figure 2 Mentawai, Indonesia geographic region with the seismic stations (pink triangles, labeled on the main map) and HR-GNSS stations (green squares, labeled on the inset map) used for this study. The epicenter of the 2010 M_w 7.8 Mentawai tsunami earthquake (yellow star), and trench (triangle line) are also indicated.

and further validated against larger historical ruptures by Small and Melgar (2023). Figure 3 shows a comparison between the mean slip model and four example stochastic models (see Figure S1 for all 30 stochas-

tic slip models). The Yue et al. (2014) model is preferred because their inversion used the most comprehensive dataset (near-field HR-GNSS recordings, teleseismic body waves, and tsunami recordings from deep-water buoys and tide gauges). This particular slip inversion is similar to the other inversions in geometry and slip directivity; however, it finds peak slip near the trench to be higher (> 20 m as opposed to < 12 m; Hill et al., 2012; Newman et al., 2011; Satake et al., 2013; U.S.G.S., 2018; Zhang et al., 2015), and it places the hypocenter at a shallower depth (~ 12 m as opposed to ~ 13 – 20 m; Satake et al., 2013; U.S.G.S., 2018; Zhang et al., 2015). Yue et al. (2014) provides a more in-depth comparison of the models. The original Yue et al. (2014) model was coarsely discretized, characterized by only 72 subfaults with strike-slip and dip-slip dimensions of $14.25 \text{ km} \times 15 \text{ km}$. Using this as an initial model, we made a finer-discretized slip model containing 2886 subfaults with strike-slip and dip-slip dimensions of $2 \text{ km} \times 2 \text{ km}$ (see Figure S2 for a comparison). We further modified the mean slip model by shifting the depth of the subfaults 3 km shallower. Because Yue et al. (2014) used the 1D velocity profile and slip inversion to generate tsunami scenarios, they added a 3 km water layer (i.e., $V_S = 0 \text{ km/s}$) to their velocity model. FakeQuakes cannot accept a V_S layer equal to 0 km/s, so this layer was removed from the velocity model, and 3 km were subtracted from the fault model depth to maintain consistency between the fault and velocity models.

The stochastic models follow a similar methodology

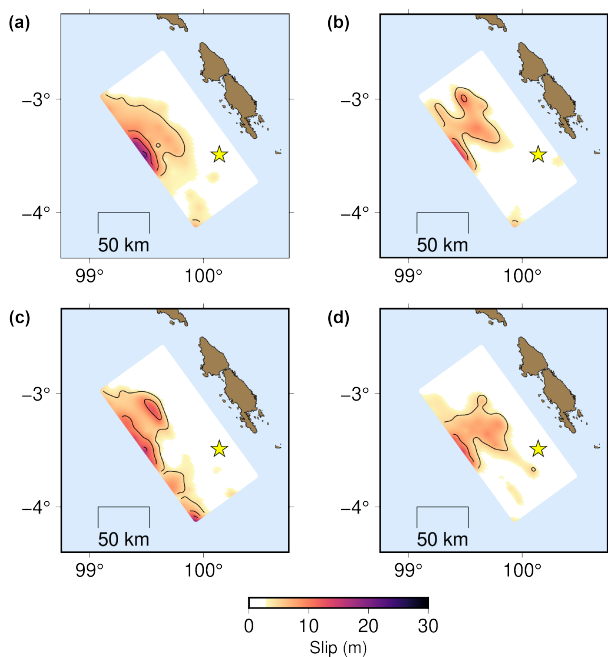


Figure 3 (a) Finely discretized slip model of the 2010 Mentawai tsunami earthquake from Yue et al. (2014). (b–d) Slip patterns generated using *FakeQuakes*, which are stochastic variations of the slip model in (a). The yellow stars indicate the epicenter.

to Mai and Beroza (2002), which assume a von Karman correlation function for slip correlation amongst subfaults. The stochastic slip vector fields are determined using Karhunen Loève (K–L) expansion (LeVeque et al., 2016), where the range of possible slip on a subfault is taken from a probability density function defined by a mean value equal to the slip on the equivalent Yue et al. (2014) model subfault. Details of this process are further described in Melgar et al. (2016) and Goldberg and Melgar (2020).

HR-GNSS displacement waveforms are generated deterministically with a 2 Hz sampling rate by combining Green’s functions computed following the matrix propagator method of Zhu and Rivera (2002) with slip on the fault. Real HR-GNSS data generally have higher noise arising from uncertainty in the position inversion during processing, electromagnetic signals in the ionosphere and troposphere, and multi-pathing (Melgar et al., 2020). Unlike seismic data, HR-GNSS noise is often in the frequency range of the signal and is thus difficult to filter out. It is reasonable then for observed PGD to have some noise bias, so we add real noise from the observed HR-GNSS recordings to the simulated HR-GNSS data for equal comparison. For each simulated recording, 512 s of noise are taken from the corresponding station observed time series, ending approximately 2.5 minutes before the origin time. The observed HR-GNSS recordings have a sampling rate of 1 Hz, thus we first decimate the simulated data for time-domain consistency when combining the two sets of data.

Strong-motion acceleration waveforms are generated semistochastically with a 100 Hz sampling rate in a

three-step process, closely following the broadband simulation methodology from Graves and Pitarka (2010, 2015). The low-frequency (< 1 Hz) portion of the waveforms are first generated deterministically using the same methodology as with the HR-GNSS waveforms. The high-frequency (> 1 Hz) portion of the waveforms are then generated in the frequency domain using Equation 1 (Graves and Pitarka, 2010),

$$A_i(f) = \sum_{j=1,M} C_{ij} S_i(f) G_{ij}(f) P(f) \quad (1)$$

where $A_i(f)$ is the amplitude spectrum for subfault i , $j = 1, M$ is the summation of different rays, C_{ij} is the radiation scale factor, $S_i(f)$ is the source spectrum, $G_{ij}(f)$ is the path attenuation term, and $P(f)$ is the site-specific high-frequency attenuation. The individual subfault spectra are summed, and stochastic white noise is added to represent the uncertainty in fine-scale heterogeneity of the subsurface. Finally, the low-frequency waveforms are double differentiated from displacement to acceleration and combined with the acceleration high-frequency waveforms using an acausal matched 4th order Butterworth filter. We deviate from Graves and Pitarka (2010) by employing a separate filter corner frequency (f_c) for the lowpass and highpass filters, rather than using a common filter f_c of 1 Hz, because we find that the latter results in an artificial notch in the broadband spectra between ~ 0.1 –1 Hz (Figure S3). The notch appears to be a result of early decay of the low-frequency spectra, which is not observed in the high-frequency spectra, rather than a result of the use of a common filter f_c . We find that using a 1 Hz lowpass filter on the low-frequency data and 0.1 Hz highpass filter on the high-frequency data minimizes the notch (Figure S4).

Figure 4 shows example simulated waveforms and their Fourier amplitude spectra (FAS) computed using *mtspec* (Krischer, 2016; Prieto et al., 2009) compared with observed for a subset of stations. These simulated data were generated using typical megathrust parameters to illustrate the need for parameter adjustment to simulate TsEs.

All the observed seismic and geodetic data contain prominent low-frequency ringing (Figures S5–S6) peaking around 0.1 Hz (Figure S7), which likely results from shallow, long duration rupture (Fukao and Kanjo, 1980; Houston, 1999). We attempted to account for this by including shallow low-velocity layers in the velocity model, but this only added low-frequency energy at certain peaks, rather than across the spectrum of missing frequencies (Figure S8). Because we see this effect for both types of instruments and at all locations, it is likely a source effect, and one we are unable to recreate using a simple 1D semistochastic model. To minimize this biasing our results, we trim the records to end at 2010–10–25T14:47:02Z (approximately 4.5 minutes after the origin time) and only evaluate acceleration FAS at frequencies above 0.1 Hz. We also exclude displacement FAS from our analyses as these are dominated by the range of frequencies characterizing the ringing and are minimally affected by the variation of parameters.

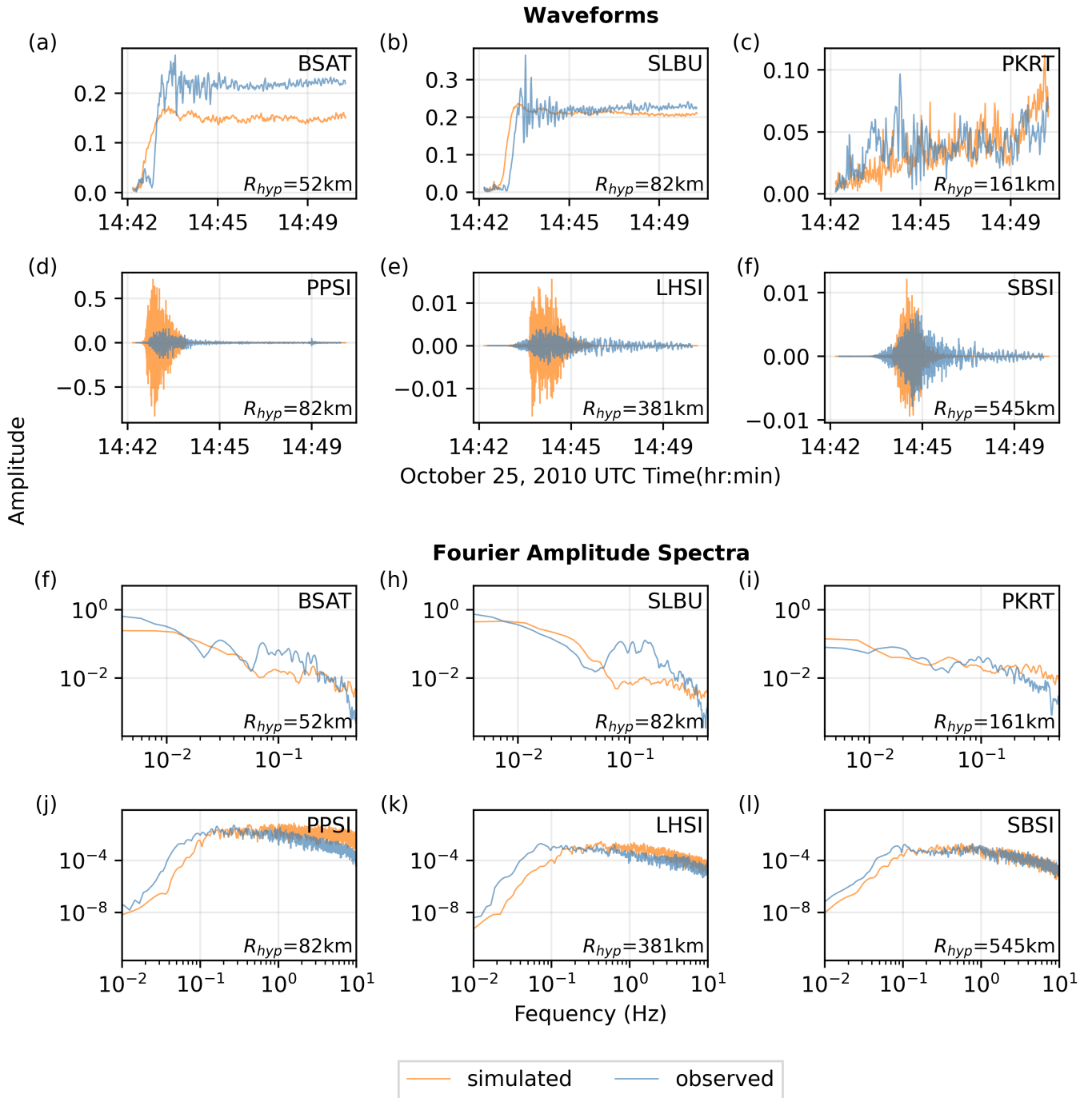


Figure 4 (a–f) Waveform comparisons between the observed (blue) data and simulated (orange) data using typical megathrust parameters for *FakeQuakes*. (a–c) Displacement waveforms for HR-GNSS stations BSAT, SLBU, and PKRT, respectively. (d–f) Acceleration waveforms for seismic stations PPSI, LHSI, and SBSI, respectively. (g–l) Fourier amplitude spectra (FAS) comparisons for the waveforms in (a–f).

3.2 Varying rupture parameters

3.2.1 Rise time

The slip duration for subfault i , or rise time (T_i), is proportional to the square root of the subfault slip (s_i) (Melgar et al., 2016) (Equation 2). Graves and Pitarka (2010) suggest a doubling of rise time at shallow depths to represent a reduction in slip speed observed with surface rupturing events. Following Melgar et al. (2016), we use a shallow depth of 10 km, rather than the 5 km proposed by Graves and Pitarka (2010) as their study fo-

cused on crustal ruptures rather than subduction interface events.

$$T_i = \begin{cases} 2ks_i^{1/2} & d < 10\text{km} \\ ks_i^{1/2} & d > 15\text{km} \end{cases} \quad (2)$$

The scaling factor, k , is applied to ensure the total mean rise time fits an empirical rise time– M_0 scaling relation. Existing rise time– M_0 relationships are biased towards typical megathrust ruptures, but TsEs deviate from the norm, having significantly longer rise times compared to their M_0 (Melgar and Hayes, 2017). As there are

only four TsEs in the Melgar and Hayes (2017) dataset, it is difficult to constrain a unique relationship for these events, but we can modify k to reflect variations in the scaling by multiplying the individual subfault rise times by a “ k -factor”. We use the Melgar and Hayes (2017) scaling relation and evaluate k -factors ranging from 1–3, which results in mean rise times ranging from ~5.4–16.2 s.

3.2.2 Rupture velocity

The rupture propagation speed has been found to be proportional to V_S , where $V_{\text{rupt}} = SF \cdot V_S$. Here, SF is the shear wave fraction. *FakeQuakes* uses this V_{rupt} as the background rupture velocity, but spatial heterogeneity in rupture propagation is accounted for by perturbing the onset times to be earlier where slip is large and later where slip is small (Graves and Pitarka, 2010, 2015; Melgar et al., 2016). We modify the V_{rupt} by adjusting the shear wave fraction at shallower depths to account for the presence of a weak shallow megathrust (Graves and Pitarka, 2010). An SF value of 0.8 is generally assumed for deeper depths (> 15 km for our model), whereas a value of 0.49 is generally assumed for shallower depths (< 10 km for our model). The shear wave fraction at depths between 10–15 km is a linear interpolation between the deep and shallow shear wave fractions. We only modify the shallow shear wave fraction (SSF) in our analyses, and we evaluate SSF s ranging from 0.3–0.49, which results in mean V_{rupt} ranging from ~1.0–1.6 km/s.

3.2.3 High-frequency stress parameter

The stress parameter, (i.e., Brune stress; Brune, 1970) is the simplest parameter to modify, because unlike rise time and V_{rupt} , it can be directly defined in the parameter file. To simulate lower stress events, we evaluate stress parameters ranging from 0.1–5.0 MPa, with 5 MPa used as the standard value for comparison.

3.3 Constraining rupture parameters

Through varying the rise time, V_{rupt} , and stress parameter, we aim to constrain the parameter space that best recreates the 2010 Mentawai TsE by minimizing the residuals of a suite of characteristic intensity measures (IMs). We want to capture the slow slip, long duration, and energy deficient nature of TsEs, whilst preserving the seismic moment. Thus, we evaluate the PGD, time to reach PGD (tPGD), PGA, and acceleration FAS bin averages. For PGD, PGA, and the binned FAS, we compute the residuals as $\ln(\text{observed}/\text{simulated})$, and for tPGD, we compute the residuals as $\text{observed} - \text{simulated}$. The acceleration FAS are binned into 10 log-spaced bins ranging 0.1–10 Hz. The upper bound of 10 Hz is a limitation of seismic data processing prior to our acquisition of the data.

4 Results

4.1 Isolated parameters

The parameters are varied initially through isolated tests, where only one parameter is varied at a time, and compared with scenarios generated using standard megathrust parameters. For these tests, only a few values of each parameter are evaluated to gauge how the IMs are affected by the varying rupture parameter, and to get a coarse idea which parameter values are ideal for modeling the Mentawai scenario. The standard stochastic simulations have a mean rise time of ~5.4 s and mean V_{rupt} of ~1.6 km/s.

For the rise time, we evaluate simulations generated using a scaling factor of $1k$, $2k$ and $3k$ (i.e., mean rise times of about 5.4, 10.8 and 16.2 s) (Figure 5). Modifying the rise time primarily influences the timing of shaking (i.e., tPGD). As expected, using the standard $1k$ results in positive tPGD residuals because the simulated data have significantly shorter moment-rates. With increased mean rise time, the mean amplitude of the residuals decreases, and if only rise time is modified, a value close to 11 s is needed to yield a tPGD residual of zero.

For the V_{rupt} , we evaluate simulations generated using SSF values of 0.49, 0.4, and 0.3 (i.e., mean V_{rupt} of 1.6, 1.3, and 1.0 km/s) (Figure 6). As with rise time, tPGD is primarily affected when varying V_{rupt} , and using the standard SSF of 0.49 results in positive tPGD residuals. The residual mean amplitude is reduced using slower rupture propagation speeds, and a V_{rupt} close to 1.3 km/s is needed to yield a tPGD residual of zero if only V_{rupt} is modified. These values for mean rise time and V_{rupt} are our endmember values of the parameter space. Because we will vary the rise time and V_{rupt} together, we expect the ideal values to fall somewhere in between a rise time of 5.4–11 s and a V_{rupt} of 1.3–1.6 km/s.

For the stress parameter, we evaluate simulations generated using stress parameters of 0.1, 1, 2, and 5 MPa, with 5 MPa being the standard value for comparison. We find that unlike rise time and V_{rupt} , the stress parameter primarily influences the high-frequency intensity measures (i.e., PGA and acceleration FAS) (Figure 7). Using a typical value of 5 MPa results in negative residuals for all the high-frequency IMs, suggesting the simulated data have more high-frequency energy than the observed. As expected, decreasing the stress parameter decreases the negative bias of the residuals, and an ideal stress value for modeling the 2010 event is close to 1 MPa when only considering PGA, or close to 2 MPa when also considering the acceleration FAS bin residuals.

4.2 Covaried parameters

The IM residual results from the previous section illustrate overall trends in the data resulting from variations in the rise time, V_{rupt} , and stress parameter. We use these results to guide the design of a larger dataset, which provides a finer sampling of the three-dimensional (3D) parameter space and a better constraint on the ideal values for simulating TsE scenarios.

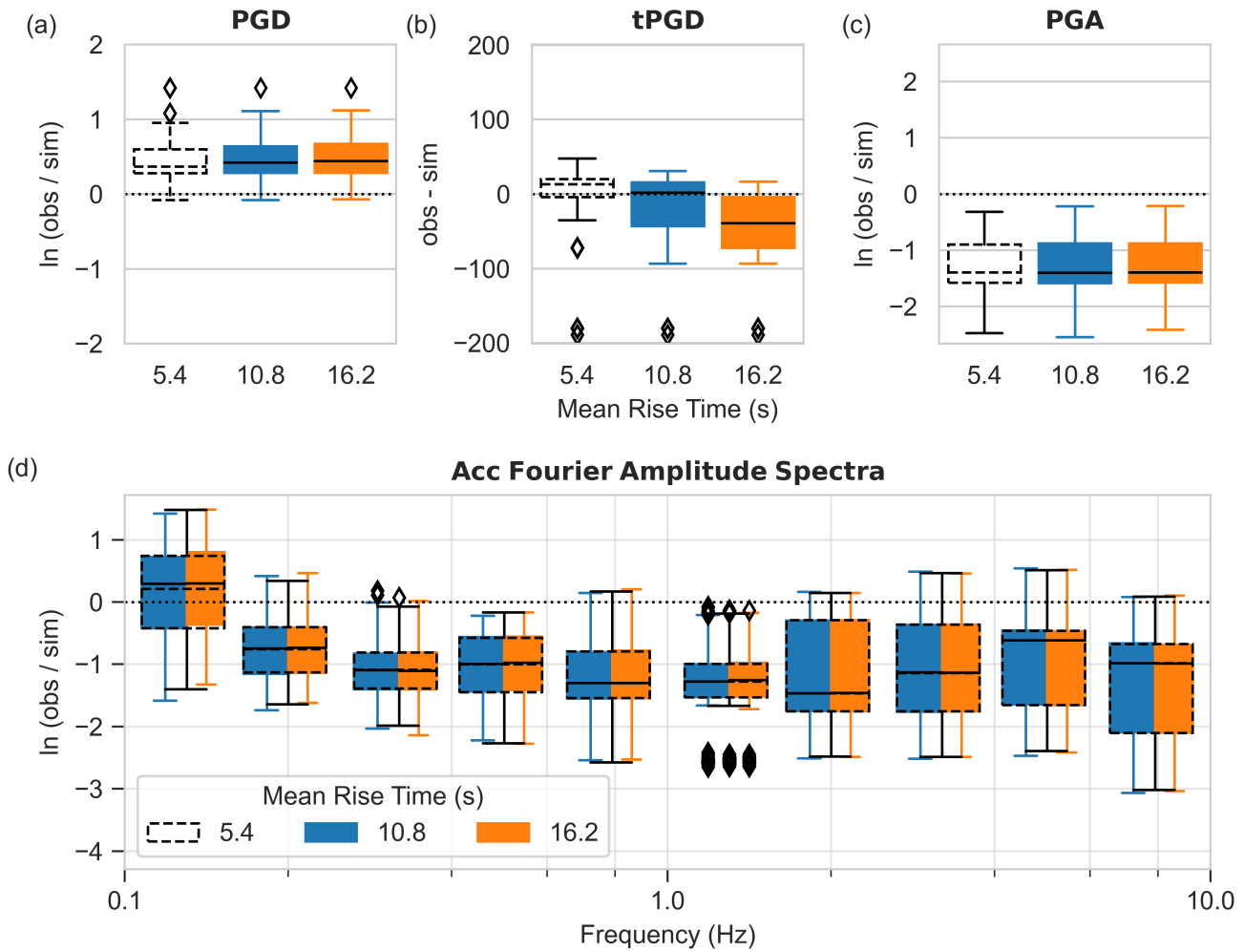


Figure 5 Initial tests showing the effects of varying rise time on (a) PGD, (b) tPGD, (c) PGA, and (d) acceleration FAS. Dashed boxplots represent residuals using standard rise time– M_0 scaling relations (k from Melgar and Hayes, 2017), resulting in a mean rise time of ~ 5.4 s. Orange boxplots represent rise times computed using $2k$, resulting in a mean rise time of ~ 10.8 s, and blue boxplots represent rise times computed using $3k$, resulting in a mean rise time of ~ 16.2 s. Diamonds within each boxplot denote outliers, and the dotted line indicates the zero-residual axial line.

We extend the full parameter space surveyed beyond the approximated endmember values to ensure resolution at the edges of the ideal parameter space. Considering the endmember rise time value is around 11 s, we run simulations spanning the rise time parameter space of 5.4 s to 12.4 s by using multiplication factors ranging from 1–2.3 at intervals of 0.1 (parameter space resolution of 0.54 s). Considering the endmember V_{rupt} is around 1.3 km/s, we run simulations spanning the V_{rupt} parameter space from 1.2 to 1.6 km/s by using SSF ranging from 0.37–0.49 at intervals of 0.03 (parameter space resolution of 0.1 km/s). Because stress parameter values can vary by orders of magnitude, we do not find it advantageous to run large suites of simulations with a fine stress parameter sampling. Instead, we run simulations using stress values of 0.1, 0.5, 1.0, 1.5, 2.0, and 3.0 MPa.

Initially, we intended to survey the full 3D parameter space by simulating data for each possible combination of rise time k -factor, SSF , and stress parameter. Findings from the isolated parameter tests (Figures 5–7) re-

veal, however, that the effects of varying rise time and V_{rupt} are essentially separate from the effects of varying the stress parameter. We instead have chosen to split the parameter space into a 2D survey of the rise time and V_{rupt} and a 1D survey of the stress parameter, which significantly decreases computation by reducing the number of parameter combinations, and allows for simpler regression of the ideal TsE parameter space.

4.3 Tsunami earthquake parameter regression

We find that individually varying the rise time, V_{rupt} , and stress parameter expectedly controls the rupture kinematics and resulting ground motions, which validates their classification as key rupture parameters for simulating TsEs. Our ultimate objective of this study is to present the mean and standard deviation of these parameters to govern simulation of TsE scenarios. Because we discretely sampled our parameter space, we obtain these values by performing Gaussian process regression (GPR) of the IM residuals.

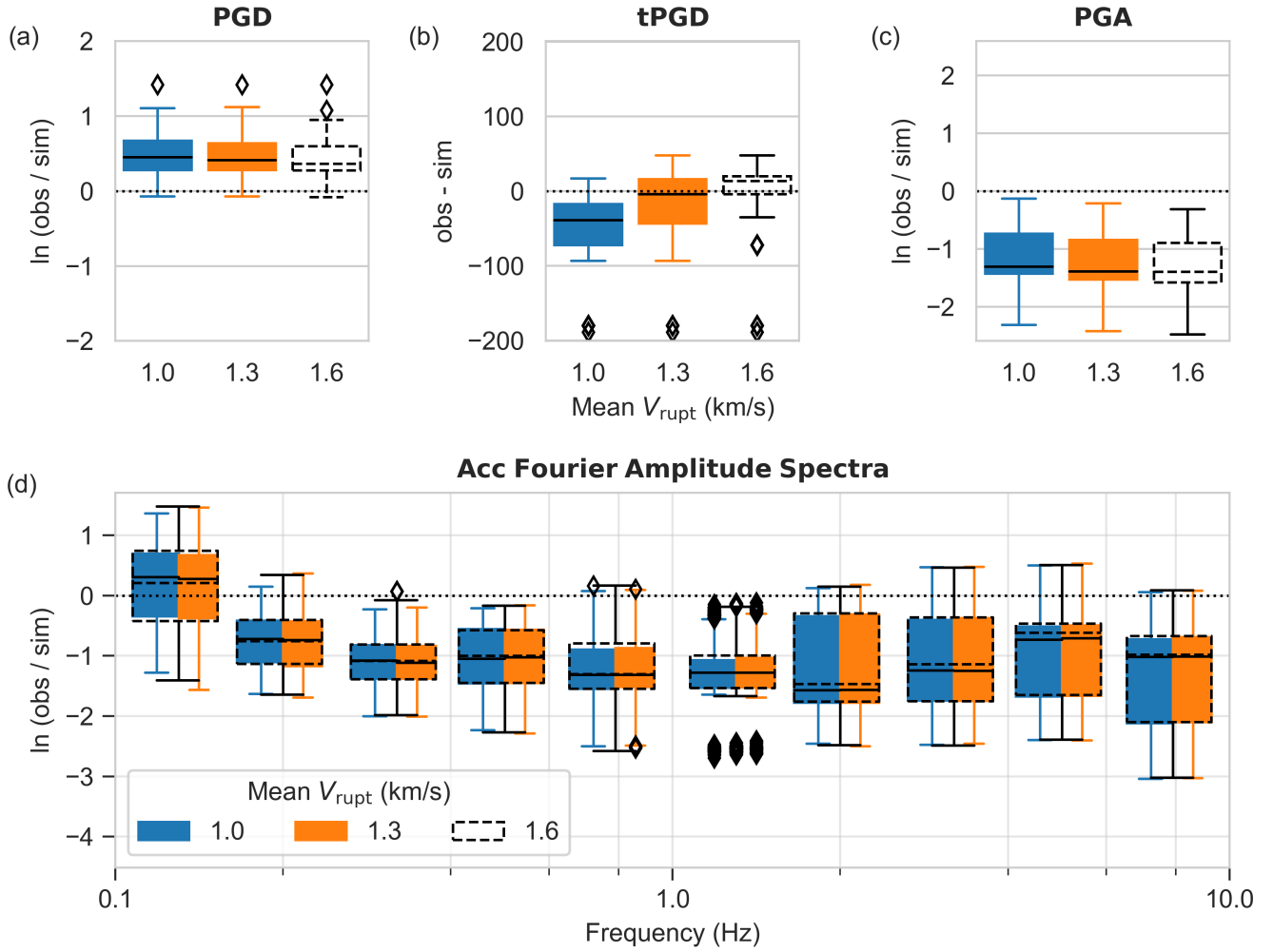


Figure 6 Initial tests showing the effects of varying V_{rupt} on (a) PGD, (b) tPGD, (c) PGA, and (d) acceleration FAS. Dashed boxplots represent residuals using a standard shallow shear wave fraction of 0.49, resulting in a mean V_{rupt} of ~ 1.6 km/s. Orange boxplots represent V_{rupt} computed using a shallow shear wave fraction of 0.4, resulting in a mean V_{rupt} of ~ 1.3 km/s, and blue boxplots represent V_{rupt} computed using a shallow shear wave fraction of 0.3, resulting in a mean V_{rupt} of ~ 1.0 km/s. Diamonds within each boxplot denote outliers, and the dotted line indicates the zero-residual axial line.

GPR is a supervised statistical learning method which computes nonparametric probabilistic models to fit a dataset. In simple terms, we assume an infinite number of functions can fit an observed set of data, and GPR computes the most probable, or mean, function along with its uncertainty. We perform a 2D GPR of the rise time- V_{rupt} parameter space and a 1D GPR of the stress parameter space using the *Scikit-learn* Python library (Pedregosa et al., 2011). The simulation IM residual results of the regression dataset are used as a prior for the GPR, along with a kernel to describe the covariance of the random process. We use the commonly used radial basis function (RBF) kernel, also known as the squared exponential kernel, due to its universality against most functions, and we set the kernel length as the maximum distance between data points.

We compute a summary residual parameter for tPGD ($\delta_{tPGD,i}$) for each event i , k -factor k , and SSF l . This is the median (med) of the tPGD residuals (δ_{tPGD}) across all j HR-GNSS stations, given the specific stochastic rupture and rupture parameter combination (Equation 3).

The median is preferred over the mean to reduce bias from potentially poorly modeled stations. This results in 2100 summary tPGD residual parameters (5 values of $SSF \times 14$ values of k -factor $\times 30$ stochastic scenarios).

$$\delta_{tPGD,i} = \text{med} \begin{bmatrix} \delta_{tPGD}(k\text{-factor}_k, SSF_l)_{j=1} \\ \vdots \\ \delta_{tPGD}(k\text{-factor}_k, SSF_l)_{j=5} \end{bmatrix} \quad (3)$$

We also compute a summary residual parameter for the high-frequency IMs ($\delta_{HF,i}$) for each event i and stress parameter (σ) k (Equation 4). Each row in the δ_{HF} vector represents a single station j residual and is computed as the average of the PGA residual (δ_{PGA}) and the mean FAS residual (δ_{FAS}). The FAS residuals are averaged prior to being averaged with δ_{PGA} to ensure equal weighting of IMs. The summary residual is the median of all j strong-motion station residuals. This results in 180 summary high-frequency residual parameters (6 values of $\sigma \times 30$ stochastic scenarios).

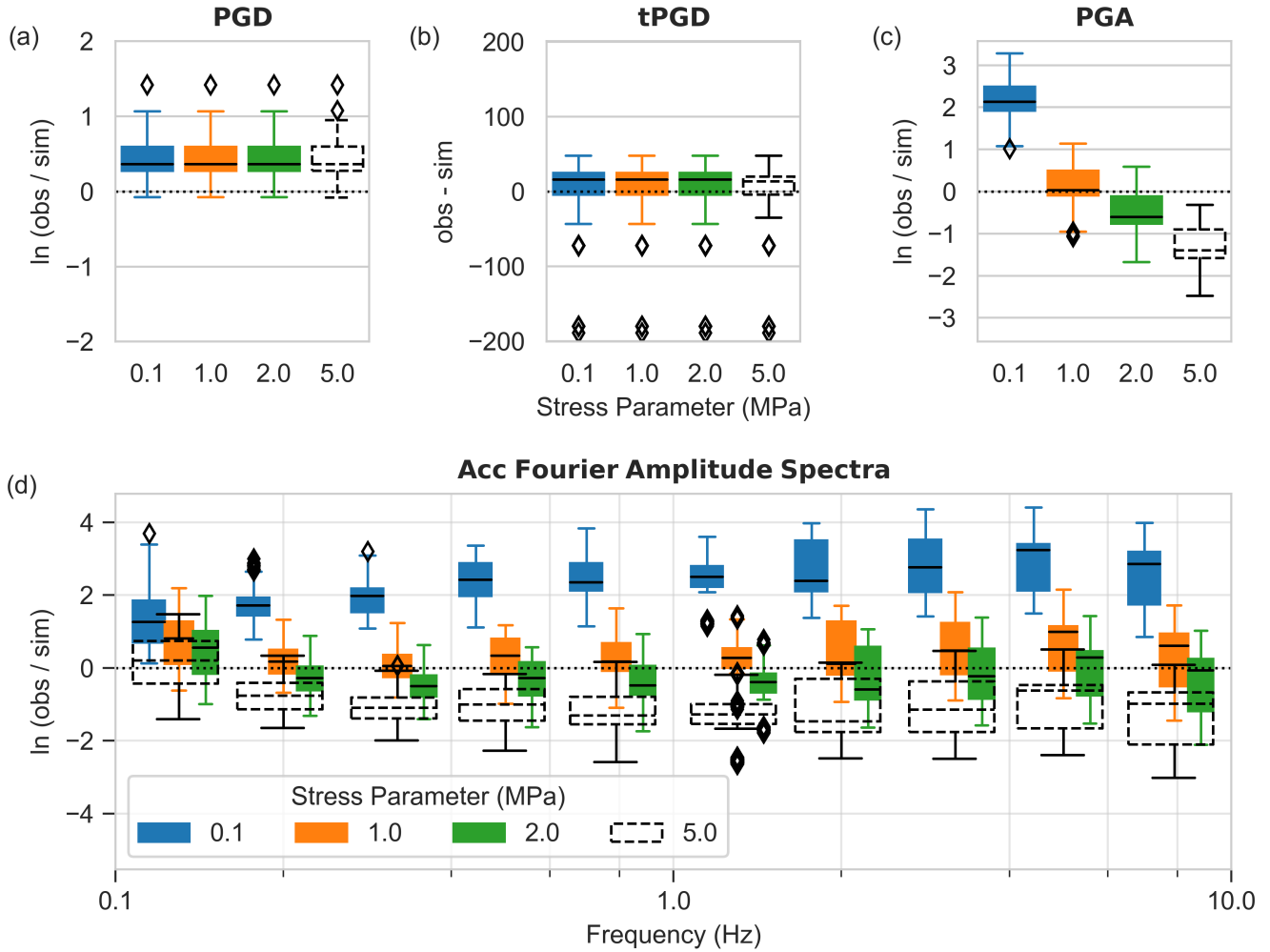


Figure 7 Initial tests showing the effects of varying the stress parameter on (a) PGD, (b) tPGD, (c) PGA, and (d) acceleration FAS. Dashed boxplots represent residuals using a standard stress parameter of 5.0 MPa. Green boxplots represent residuals using a stress parameter of 2.0 MPa, orange boxplots represent residuals using a stress parameter of 1.0 MPa, and blue boxplots represent residuals computed using a stress parameter of 0.1 MPa. Diamonds within each boxplot denote outliers, and the dotted line indicates the zero-residual axial line.

$$\delta_{\text{HF},i} = \text{med} \begin{bmatrix} 0.5 \left(\delta_{\text{PGA}}(\sigma_k) + \overline{\delta_{\text{FAS}}(\sigma_k)} \right)_{j=1} \\ \vdots \\ 0.5 \left(\delta_{\text{PGA}}(\sigma_k) + \overline{\delta_{\text{FAS}}(\sigma_k)} \right)_{j=9} \end{bmatrix} \quad (4)$$

The results of the 2D GPR of the rise time and V_{rupt} and the 1D GPR of the stress parameter are shown in Figure 8. The range of parameter combinations most likely to result in $\delta_{\text{tPGD}} = 0$ s is nearly linear and extends from a rise time- V_{rupt} combination of about 5.4 s-1.26 km/s to 12.0 s-1.60 km/s. The standard deviations returned for the 2D regression highlighted in Figure 8b are relatively uniform because they are conditioned upon the spatial sampling of the prior, which was evenly sampled by our dataset. Although uncertainty estimates are a desirable feature of GPR, these provide a measure of uncertainty in the values of the function, rather than uncertainties in parameter coordinates resulting in a single function value. Therefore, we present the standard deviation lines in Figure 8a as the standard deviation of

the GPR mean predictions. Fitting a line to the linear segment of the zero-residual line, we obtain Equation 5, which can be used to select reasonable values of rise time (T_a) and V_{rupt} for simulating TsEs.

$$V_{\text{rupt}} = 0.08(T_a) + 0.31 \pm 0.16 \text{ km/s} \quad (5)$$

The uncertainty of ± 0.16 km/s is taken as the approximate vertical distance between the one-standard deviation lines and the zero-residual line.

In Figure 8c, positive residuals indicate stress parameters resulting in strong-motion waveforms lacking high-frequency energy compared to the observed 2010 Mentawai event, whereas negative residuals indicate stress parameters biased towards high-frequency energy. The Nelder-Mead method of the *SciPy* optimization Python library (Virtanen et al., 2020) is used to solve for the best fit stress parameter resulting in a mean δ_{HF} of zero, which is found to be 1.2 MPa. As with the 2D regression, we present the standard deviation in stress parameter as the standard deviation of the GPR mean predictions.

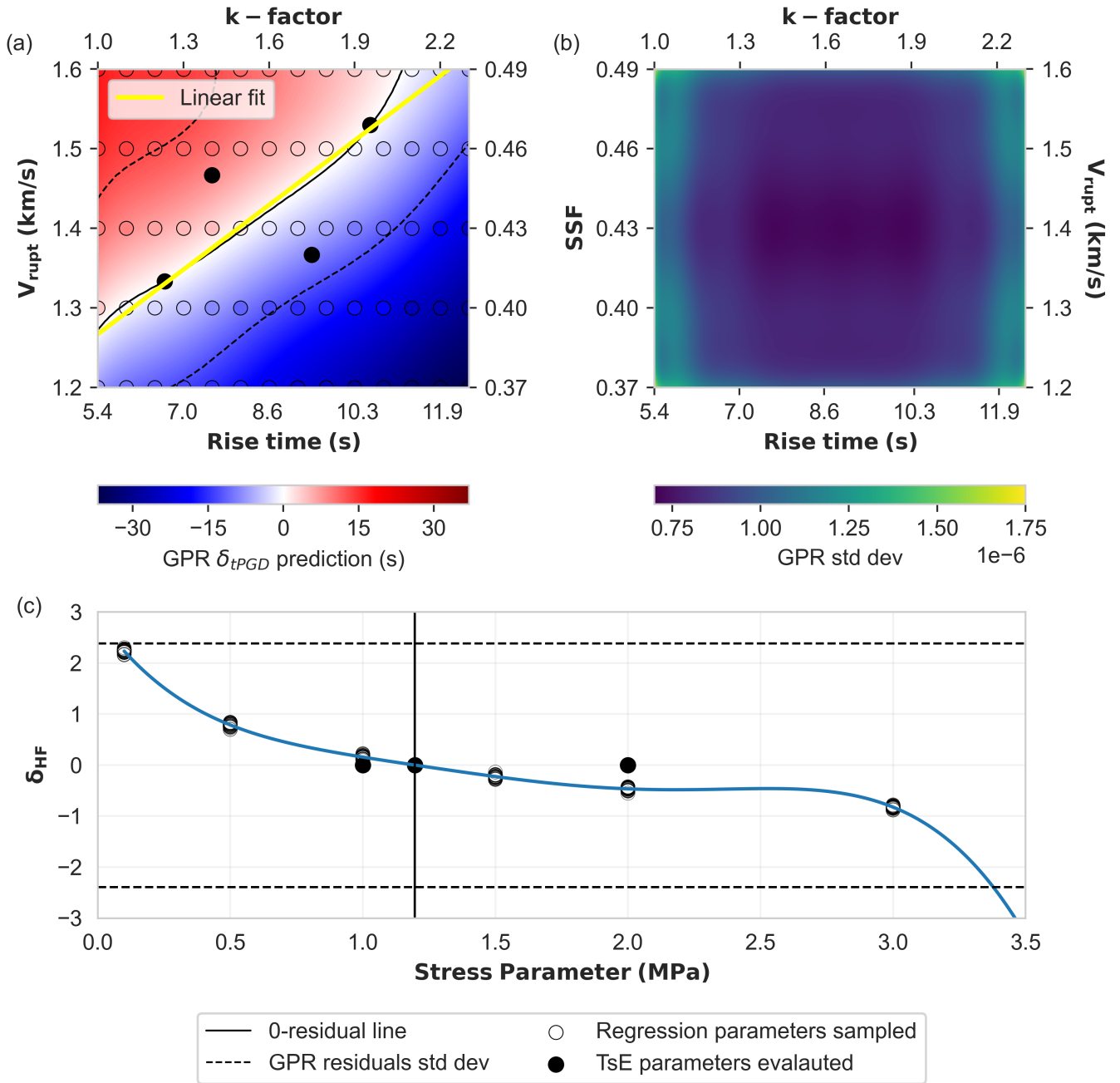


Figure 8 (a) 2D Gaussian process regression (GPR) of tPGD residuals (δ_{tPGD}) of simulated data using varying rise time and V_{rupt} simulation parameters (k -factor and SSF , respectively). Red regions suggest parameter combinations resulting in too early tPGD, whereas blue regions suggest parameter combinations resulting in too late tPGD. (b) Standard deviation of the GPR mean function in (a). (c) 1D GPR of high-frequency intensity measure residuals (i.e., mean of PGA and acceleration FAS residuals) for the simulation stress parameter. The mean function and 95% confidence are indicated by the solid blue line and shaded regions, respectively. For all subplots, the solid black line represents the parameter(s) where the mean has a residual of zero, and the dashed black lines represent \pm one standard deviation of the GPR predictions. The open circles indicate the parameter space surveyed by the simulation dataset, where each discrete data point illustrates the median residuals for each of the 30 stochastic events. The filled black circles indicate the tsunami earthquake (TsE) parameter space surveyed in a final dataset, but were not used for the GPR.

Stress parameter values within approximately ± 1.7 MPa result in residuals within the one-standard deviation lines; thus, we present Equation 6 for selecting a reasonable TsE stress parameter.

$$\sigma = 1.2 \pm 1.7 \text{ MPa} \tag{6}$$

In theory, we expect simulations run with parameters falling within one-standard deviation of the mean model to be reasonably representative of a real TsE. To validate this, the results of the two regressions are used to inform the parameters of a final dataset representing likely TsE scenarios. We generate a new set of 30 stochastic slip models for this dataset following simi-

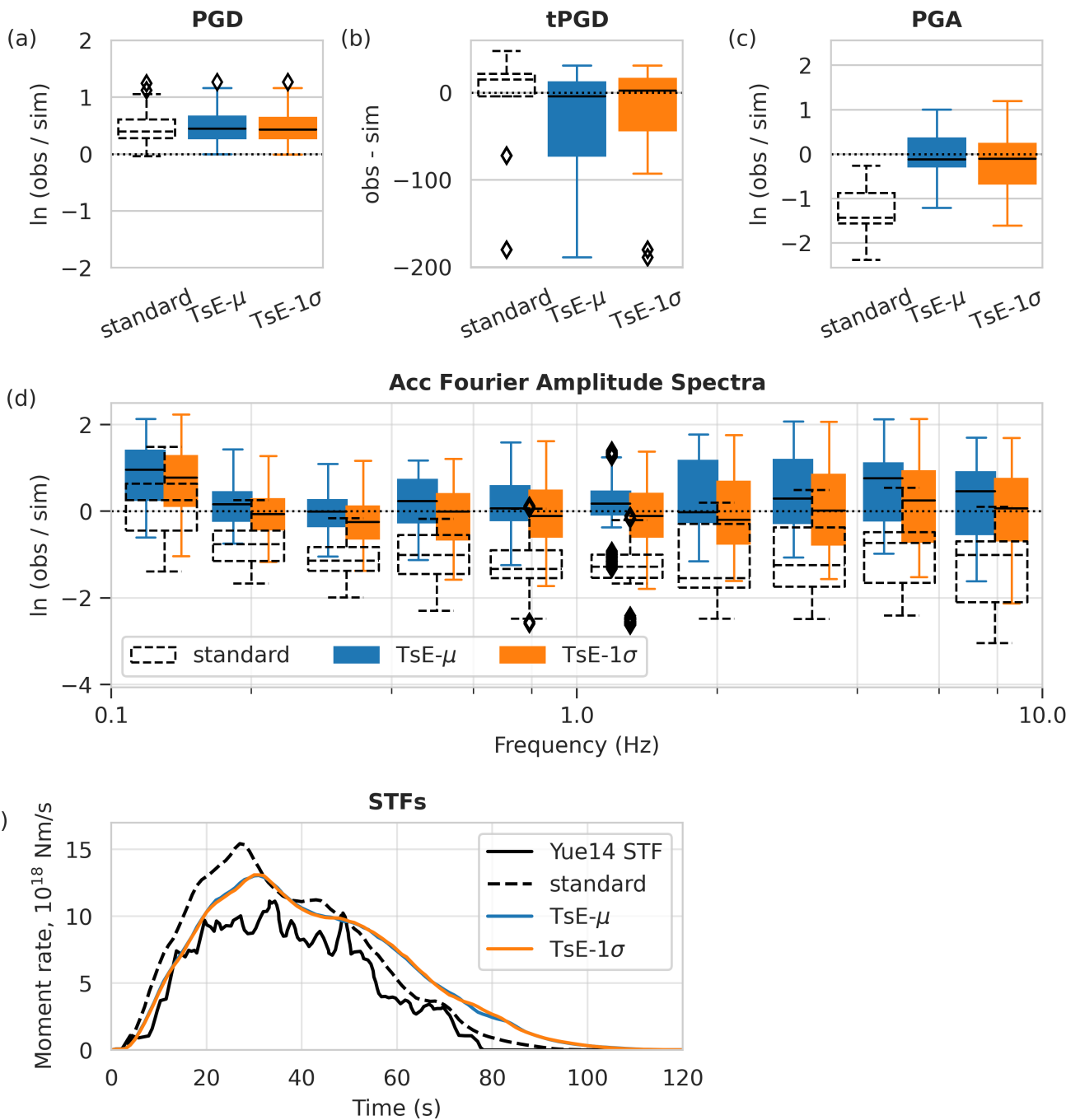


Figure 9 Intensity measure residual analyses comparing observed and simulated data generated using standard parameters, mean values from the TsE parameter regression (TsE- μ), and values within one standard deviation of the mean from the TsE parameter regression (TsE- 1σ) for (a) PGD, (b) tPGD, (c) PGA, and (d) acceleration FAS. (e) We also compare the average STFs for the simulated data using TsE parameters and standard parameters with a STF computed using observed data (Yue et al., 2014). All IMs and the STFs better fit observed data when using recommended TsE parameters.

lar standard practices of machine learning where separate data are used for testing and training. This TsE dataset consists of six parameter configurations: two using mean values from the zero-residual GPR predictions, and four using values within the one-standard deviation bounds. Table 1 lists the values of parameters used for these simulations, and the parameter space coordinates of the rise time, V_{rupt} , and stress parameter are indicated on the regression plots in Figure 8. We find that the simulated TsE scenarios adequately model

the observed IMs of the Mentawai event, as indicated by the near-zero residuals of the IMs in Figure 9. The source time functions (STFs) of the simulations are also evaluated, and we find reasonable similarity with the observed STF.

Parameters ^a	k-factor ^b	Rise time ^c (s)	SSF ^d	V_{rupt} ^e (km/s)	Stress parameter (MPa)
μ -a	1.23	6.66	0.41	1.32	1.2
μ -b	1.95	10.54	0.47	1.51	1.2
1 σ -a	1.40	7.56	0.45	1.45	1.0
1 σ -b	1.40	7.56	0.45	1.45	2.0
1 σ -c	1.75	9.44	0.42	1.35	1.0
1 σ -d	1.75	9.44	0.42	1.35	2.0

Table 1 Tsunami earthquake simulation rupture parameters.

^a Parameters μ -a and μ -b refer to two sets of parameter combinations using mean values of the rupture parameters. Parameters 1 σ -a to 1 σ -d refer to four sets of parameter combinations using values of rupture parameters within one standard deviation.

^b Scaling factor applied to subfault rise times.

^c Mean subfault risetime averaged over the 30 stochastic scenarios.

^d Shear wave fraction applied at shallow depths to modify rupture velocity.

^e Mean rupture velocity averaged over the 30 stochastic scenarios.

5 Discussion

5.1 Simulation limitations

Through various permutations of the rise time, V_{rupt} , and stress parameter, we capture key features of the observed data in the simulations, namely slow moment-rate (i.e., large tPGD) and high-frequency deficiency (i.e., low PGA and high-frequency amplitudes of acceleration FAS). There are, however, aspects of the data we are unable to reconstruct. As previously addressed, the observed displacement and acceleration data both exhibit significant ringing, which is likely a source effect due to its presence in recordings of all HR-GNSS and strong-motion stations. It is unclear whether this is a unique property of all TsEs, a result of rupturing the compliant wedge in an accretionary setting, or an isolated occurrence due to the complex 3D crustal structure of the Mentawai region. Until more near-field TsE recordings exist or a high-resolution and high-fidelity velocity model is available in the region, we cannot definitively answer this question. Regardless, this appears to have little effect on the IMs necessary for near-real-time analysis.

Interestingly, a systematic under-generation of PGD is still observed for all HR-GNSS simulated data, regardless of rupture parameter configuration. Albeit, the scale of the discrepancy is minute, with the residuals averaging less than 0.5 natural log unit. It is possible that the source of the ringing in the observed GNSS data also amplified observed PGD. However, this phenomenon has been observed in other studies employing similar 1D forward model methodology (e.g., [Fadugba et al., 2024](#); [Melgar et al., 2016](#)). [Fadugba et al. \(2024\)](#) find that using 3D rather than 1D velocity structure significantly improves PGD residuals, as complex 3D effects are not fully captured by the simple 1D profiles.

The selection of a velocity model has direct implications on results from inversion and forward modeling studies, such as this one. It not only defines the elastic properties of the accretionary prism and crust, which influences the resulting amplitude of shallow slip, but also controls the kinematics of the rupture and time-dependent ground motions ([Bilek and Lay, 1999](#); [Kuncoro et al., 2023](#); [Lotto et al., 2017](#); [Ma and Nie, 2019](#); [Sal-](#)

[larès et al., 2021](#); [Qiu and Barbot, 2022](#); [Yao et al., 2013](#)). The implementation of a 1D model does not consider wedge geometry, although [Kuncoro et al. \(2023\)](#) found that variations in physical properties, rather than wedge dimension, had a stronger influence on coseismic deformation when looking at the Mentawai segment of the Sumatra subduction zone. Another limitation is that the 1D velocity model is considered uniform across the entire region. We should expect the structure to differ between the subduction interface (characterized by cold, dense oceanic crust and weak accretionary material) from that of less dense crust where the stations are located. 3D models can better capture these lateral variations, but they are more computationally expensive to run. Thus, their implementation reduces the size of the resulting dataset—a significant loss in the field of early warning where large datasets are desired for robust testing. Given our derived TsE rupture parameters are within the expected range and produce ground motions that closely match those observed for the 2010 Mentawai event, we maintain that the simulation results from this study are a valuable input for future tsunami early warning testing.

5.2 Comparison with previous inversion studies

Through stochastic forward simulations exploring a range of rupture parameters, we have characterized source features of the 2010 Mentawai event, including the rupture parameters rise time, V_{rupt} , and stress parameter, as well as the source duration. We find that our results are consistent with source inversion studies of the Mentawai event. Although we did not solve for a single rise time and V_{rupt} , we obtained a range of values capable of replicating the observed tPGD. [Melgar and Hayes \(2017\)](#) report the mean rise time to be ~ 8 s, and other studies have found the V_{rupt} to range from ~ 1.25 – 2 km/s (e.g., [Lay et al., 2011](#); [Newman et al., 2011](#); [Yue et al., 2014](#); [Zhang et al., 2015](#)). These parameter configurations fall within one standard deviation of the mean prediction for zero residuals from [Figure 8](#). We find that a simulation stress parameter of 1.2 MPa best captures the PGA and acceleration FAS amplitudes, which is slightly overestimated compared to the 0.9 MPa

estimate by Yue et al. (2014). However, strong-motion FAS were not considered in their inversion. If we were to perform the 1D GPR solely on PGA, we would likely obtain a similar result. The average source durations of the TsE simulations from the final dataset are about 110 s, which is well within the 80–125 s range of other studies (e.g., Lay et al., 2011; Newman et al., 2011; Yue et al., 2014; Zhang et al., 2015).

5.3 Near real-time discrimination

A near-real-time discrimination algorithm using PGD- and PGA-derived magnitudes was proposed by Sahakian et al. (2019) for distinguishing TsEs. This algorithm builds upon the premise that TsEs are energy deficient, thus having characteristically low PGA compared to PGD. The magnitude of shaking estimated using PGA (M_{PGA}) would underestimate the moment magnitude, which can be approximated using PGD (M_{PGD}). In their study, they computed $M_{\text{PGA}} - M_{\text{PGD}}$ for a handful of moderate to large events, including the 2010 Mentawai TsE, and found that typical events had an average $M_{\text{PGA}} - M_{\text{PGD}}$ of zero, whereas the Mentawai event had a $M_{\text{PGA}} - M_{\text{PGD}}$ close to -1 . Here, we perform the analysis on the final TsE dataset to ensure a similar result with the simulations.

M_{PGD} is computed by minimizing a least squares problem governed by a PGD ground-motion model (GMM). Rather than predicting PGD given some magnitude and distance, we invert for the magnitude using known PGD and distance parameters for the set of HR-GNSS stations. We use the Goldberg et al. (2021) model because it employs the generalized mean rupture distance (R_p) as the distance metric, which better describes a station's relation to the primary slip of an event compared to hypocentral distance and is better suited for close distances to a finite rupture compared to minimum distance metrics. This model was also regressed on a dataset consisting of both observed data and data simulated using *FakeQuakes*.

Models for PGA are functionally more complex than for PGD, and the parameters used are not as well constrained as magnitude or distance, especially in a near-real-time application. We instead determine M_{PGA} by finding the event magnitude whose GMM mean PGA and variance best fit the simulated PGA. We do this by first predicting PGA using the Zhao et al. (2006) GMM for a wide range of earthquake magnitudes (M_w 5.5–8.5 sampled every 0.1 magnitude unit). We next compute PGA residuals for each of the trial magnitudes. Finally, we perform a series of two-sample Kolmogorov–Smirnov (K-S) tests to determine which magnitude best represents the simulated PGA. The two datasets used consist of the PGA residuals and a random distribution with a mean of zero and a standard deviation equal to the GMM standard deviation. If the simulated PGA are well represented by a GMM given a certain trial magnitude, we should expect the residuals to have a zero-average. The K-S test returns a p -value, which indicates the likelihood the two datasets come from different distributions. Once the p -value reaches a minimum significance value of 0.05 for a trial magni-

tude, we consider that magnitude to be M_{PGA} (See Figure S9 for an example plot).

We obtain M_{PGD} values a little lower than that computed by Sahakian et al. (2019) (Figure 10a), and M_{PGD} for both studies underestimate the true moment magnitude (M_{PGD} 7.2–7.6 compared to M_w 7.8), but that is likely due to limitations of the point source assumption in GMMs. As anticipated, M_{PGA} values for the simulations are appreciably lower than M_{PGD} , although they are also slightly lower than that computed by Sahakian et al. (2019) (Figure 10b). Despite the simulated magnitude estimates being lower than the observed estimates, the resulting $M_{\text{PGA}} - M_{\text{PGD}}$ values for the simulations average around -1.5 (Figure 10c), similar to that computed by Sahakian et al. (2019). Two-sample K-S tests between the TsE simulation $M_{\text{PGA}} - M_{\text{PGD}}$ values and $M_{\text{PGA}} - M_{\text{PGD}}$ values for dissimilar event types (i.e., observed typical earthquakes; standard parameter simulations) result in extremely small p -values (10^{-18} and 10^{-41} , respectively), which signifies the simulated TsE scenarios are statistically different from standard earthquakes. Two-sample K-S tests between simulated and observed $M_{\text{PGA}} - M_{\text{PGD}}$ for similar event types (i.e., standard parameter simulations and observed typical earthquakes; TsE simulations and a distribution centered on the observed Mentawai value) are also small (10^{-7} and 10^{-9} , respectively), yet significantly higher than the p -values for K-S tests between TsE simulations and standard earthquakes, which suggests they are more statistically similar. Thus, we find simulations generated using recommended TsE parameters successfully capture the IM-derived magnitude disparity expected in near-real-time analysis of TsEs, which further validates their use for improving tsunami early warning capabilities.

5.4 Extrapolation to other regions

Although the results from this study are based solely on one event, we are optimistic that they can be applied to simulate average tsunami earthquake-type events in other regions. TsEs have characteristic features that differ strongly from typical earthquakes, irrespective of the geometry and physical properties of the subduction zone. Using semistochastic kinematic models, the rise time, V_{rupt} , and stress parameters can be directly tuned to yield such features. This is also the first step in making progress towards improving our understanding of such rare events, and the ability of tsunami early warning systems to recognize them as a severe threat. As more events are expectedly recorded in the future, we will be able to further constrain these values.

Curated TsE simulation datasets could be used to test early warning capabilities, especially in regions with a history of multiple TsEs (e.g., Sunda, Peru–Chile, and Japan trenches). Although not every subduction zone has recorded a TsE, we cannot rule out the possibility of a future occurrence. It could thus be valuable to simulate TsEs in these gap regions. The Cascadia Subduction Zone is of particular interest as its morphology and wedge structure imply a high tsunami runup potential for a rupture propagating into the shallow domain (Qiu and Barbot, 2022). Joint tsunami modeling stud-

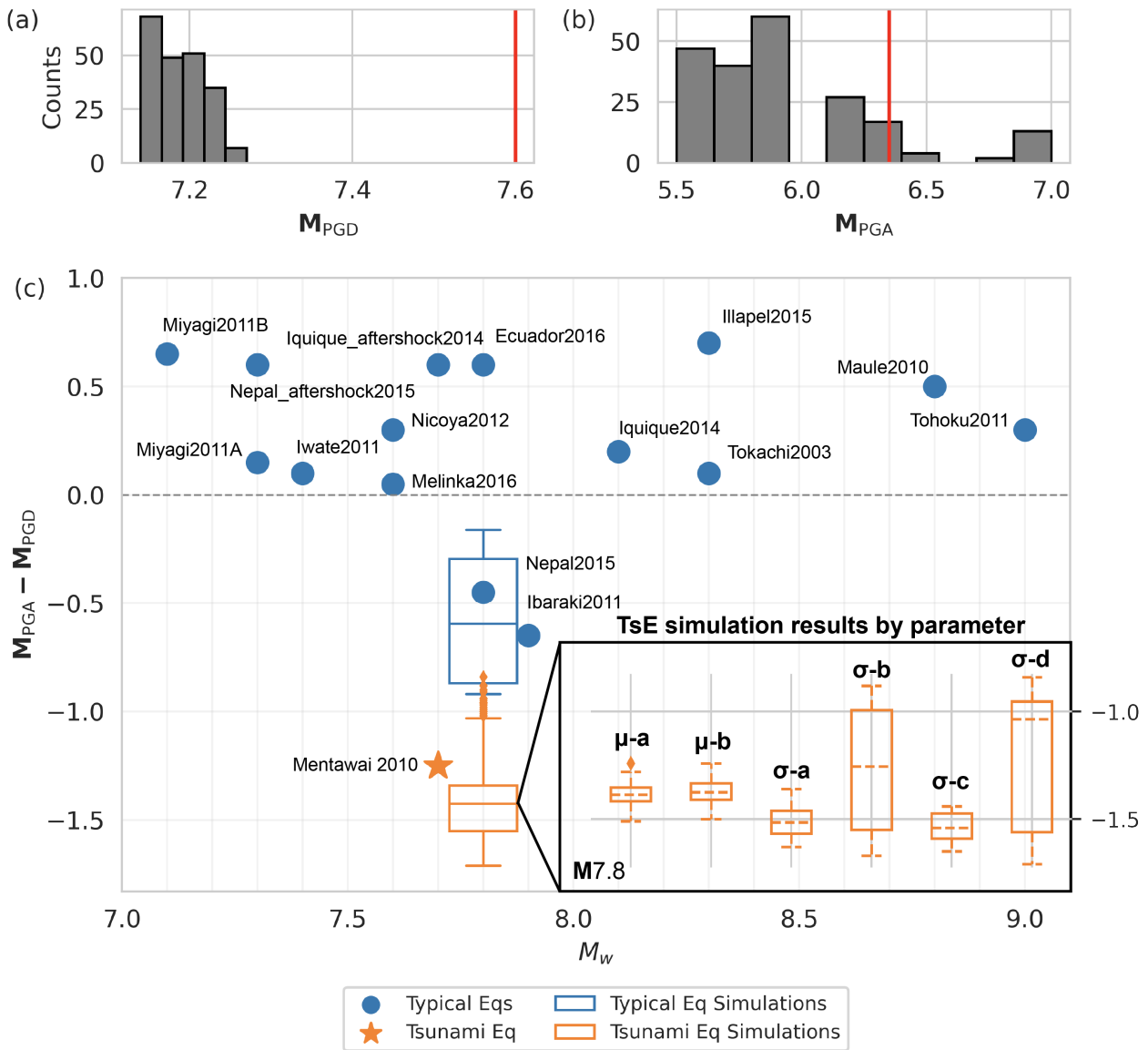


Figure 10 (a–b) Histograms of M_{PGD} and M_{PGA} , respectively, for simulations of the 2010 Mentawai tsunami earthquake. Red lines indicate the 2010 Mentawai magnitude value calculated by Sahakian et al. (2019) using observed data. (c) $M_{PGA} - M_{PGD}$ for 15 observed events (from Sahakian et al., 2019) and simulations of the 2010 Mentawai tsunami earthquake using six different TsE rupture parameter combinations, as well as standard megathrust parameters. Each boxplot in the expanded frame represents values for 30 stochastic events. μ -a and μ -b are parameter combinations using mean values of the mean Gaussian process regression resulting in summary residual parameters δ_{TPGD} and δ_{HF} of zero (i.e., along the solid black lines in Figure 8). 1σ -a, 1σ -b, 1σ -c, and 1σ -d are parameter combinations using values within one standard deviation of the total residuals (i.e., within the dashed black lines in Figure 8). The values for each parameter combination are given in Table 1.

ies could illuminate expected hazards from a potential TsE and provide region-specific constraints on the alert time needed before tsunami inundation.

6 Conclusions

TsEs are a uniquely challenging problem for both earthquake and tsunami early warning as they rupture up-dip of the traditionally seismogenic region (Wirth et al., 2022), result in unusually weak shaking even in the near-field, and produce tsunami amplitudes on par with some of the largest earthquake-generated tsunamis in history. Unassuming to seismic-driven earthquake early warning systems and magnitude-driven tsunami

early warning systems, previous TsEs have not allowed for ample warning prior to tsunami inundation and are highly destructive to communities in their wake. The rarity of these events further complicates the problem, as minimal data exist to help better understand the underlying physics governing the ruptures and develop algorithms capable of discriminating TsEs in near-real-time. Using near-field observations and simulated seismogeodetic data, we establish constraints on acceptable rupture parameter values for use in simulating TsE scenarios as a supplement for real data.

Using *FakeQuakes* forward modeling, we constrain ideal rupture parameter configurations, which successfully recreate the near-field ensemble of ground mo-

tions for the 2010 Mentawai TsE. Our intent is for this configuration (Figure 8; Equations 5–6) to be used to generate TsE scenarios in other regions around the world to aid in the assessment of tsunami early warning systems in the case of an unexpected tsunami earthquake.

Acknowledgements

This work was supported by the NASA ROSES grant 80NSSC21K0841, and USGS grants G19AP00071 and G23AP00048. We thank Earth Observatory of Singapore, Nanyang Technological University (EOS-NTUS) and the Agency for Meteorology, Climatology, and Geophysics of Indonesia (BMKG) for collecting and sharing geophysical data for the 2010 Mentawai earthquake. We are grateful to Christine Ruhl and Dara Goldberg for providing and processing the HR-GNSS data, and to Muzli Muzli for providing processed strong-motion data for the Mentawai event. We express special thanks to Ben Farr for providing valuable insight on statistical analyses, including Gaussian process regression. We also acknowledge the thorough and constructive remarks provided by two anonymous reviewers, which undoubtedly improved the quality of this paper.

Data and code availability

Observed data for the 2010 Mentawai tsunami earthquake were obtained from Muzli Muzli of the BMKG and from the Ruhl et al. (2019) database. These data were recorded by HR-GNSS instruments operated by EOS-NTUS and strong-motion stations operated by the BMKG. Simulated data were generated using *FakeQuakes*, and the codes are available online at <https://github.com/dmelgarm/MudPy>. Inversion data used for simulating the Mentawai event were obtained from Yue et al. (2014). Rupture files and waveforms for the simulations can be accessed via our online Zenodo dataset (Nye et al., 2024). Maps were produced using the Generic Mapping Tools software (Wessel et al., 2019) with a digital elevation model downloaded from GMT-SAR (Sandwell et al., 2011), and all analyses were completed with in-house code, available online at <https://github.com/taranye96/tsuquakes>. This includes a parameter configuration file for simulating data with *FakeQuakes*, and all major codes used for processing and analysis of the data and figure generation. The electronic supplement contains more figures illustrating the slip models, an analysis on the matched filter technique implemented, example effects of varying the shallow velocity structure, and an example of M_{PGA} estimation.

Competing interests

The authors have no competing interests.

References

Atkinson, G. M. and Macias, M. Predicted ground motions for great interface earthquakes in the Cascadia Subduction Zone. *Bul-*

letin of the Seismological Society of America, 99(3):1552–1578, June 2009. doi: 10.1785/0120080147.

Bilek, S. L. and Lay, T. Rigidity variations with depth along interplate megathrust faults in subduction zones. *Nature*, 400(6743): 443–446, July 1999. doi: 10.1038/22739.

Bilek, S. L. and Lay, T. Tsunami earthquakes possibly widespread manifestations of frictional conditional stability. *Geophysical Research Letters*, 29(14), July 2002. doi: 10.1029/2002gl015215.

Bilek, S. L., Engdahl, E. R., DeShon, H. R., and El Hariri, M. The 25 October 2010 Sumatra tsunami earthquake: Slip in a slow patch. *Geophysical Research Letters*, 38(14), July 2011. doi: 10.1029/2011gl047864.

Bilek, S. L., Rotman, H. M. M., and Phillips, W. S. Low stress drop earthquakes in the rupture zone of the 1992 Nicaragua tsunami earthquake. *Geophysical Research Letters*, 43(19), Oct. 2016. doi: 10.1002/2016gl070409.

Brune, J. N. Tectonic stress and the spectra of seismic shear waves from earthquakes. *Journal of Geophysical Research*, 75(26): 4997–5009, Sept. 1970. doi: 10.1029/jb075i026p04997.

Clift, P. and Vannucchi, P. Controls on tectonic accretion versus erosion in subduction zones: Implications for the origin and recycling of the continental crust. *Reviews of Geophysics*, 42(2), Apr. 2004. doi: 10.1029/2003rg000127.

Collings, R., Lange, D., Rietbrock, A., Tilmann, F., Natawidjaja, D., Suwargadi, B., Miller, M., and Saul, J. Structure and seismogenic properties of the Mentawai segment of the Sumatra subduction zone revealed by local earthquake traveltime tomography. *Journal of Geophysical Research: Solid Earth*, 117(B1), Jan. 2012. doi: 10.1029/2011jb008469.

Dieterich, J. H. Modeling of rock friction: 1. Experimental results and constitutive equations. *Journal of Geophysical Research: Solid Earth*, 84(B5):2161–2168, May 1979. doi: 10.1029/jb084ib05p02161.

Du, Y., Ma, S., Kubota, T., and Saito, T. Impulsive tsunami and large runup along the Sanriku coast of Japan produced by an inelastic wedge deformation model. *Journal of Geophysical Research: Solid Earth*, 126(8), Aug. 2021. doi: 10.1029/2021jb022098.

Duputel, Z., Tsai, V. C., Rivera, L., and Kanamori, H. Using centroid time-delays to characterize source durations and identify earthquakes with unique characteristics. *Earth and Planetary Science Letters*, 374:92–100, July 2013. doi: 10.1016/j.epsl.2013.05.024.

Eberhart-Phillips, D. and Bannister, S. 3-D imaging of the northern Hikurangi subduction zone, New Zealand: variations in subducted sediment, slab fluids and slow slip. *Geophysical Journal International*, 201(2):838–855, Mar. 2015. doi: 10.1093/gji/ggv057.

Eberhart-Phillips, D., Bannister, S., and Ellis, S. Imaging P and S attenuation in the termination region of the Hikurangi Subduction Zone, New Zealand. *Geophysical Journal International*, 198(1):516–536, May 2014. doi: 10.1093/gji/ggu151.

Fadugba, O., Sahakian, V., Melgar, D., Rodgers, A., and Shimony, R. The Impact of the three-dimensional structure of a subduction zone on time-dependent crustal deformation measured by HR-GNSS. *Seismica*, 3(1), May 2024. doi: 10.26443/seismica.v3i1.887.

Felix, R. P., Hubbard, J. A., Moore, J. D. P., and Switzer, A. D. The role of frontal thrusts in tsunami earthquake generation. *Bulletin of the Seismological Society of America*, 112(2):680–694, Nov. 2021. doi: 10.1785/0120210154.

Fukao, Y. Tsunami earthquakes and subduction processes near deep-sea trenches. *Journal of Geophysical Research: Solid Earth*, 84(B5):2303–2314, May 1979. doi: 10.1029/jb084ib05p02303.

- Fukao, Y. and Kanjo, K. A zone of low-frequency earthquakes beneath the inner wall of the Japan Trench. *Tectonophysics*, 67 (1–2):153–162, Aug. 1980. doi: 10.1016/0040-1951(80)90170-5.
- Geersen, J. Sediment-starved trenches and rough subducting plates are conducive to tsunami earthquakes. *Tectonophysics*, 762:28–44, July 2019. doi: 10.1016/j.tecto.2019.04.024.
- Goldberg, D. E. and Melgar, D. Generation and validation of broadband synthetic P waves in semistochastic models of large earthquakes. *Bulletin of the Seismological Society of America*, 110(4):1982–1995, July 2020. doi: 10.1785/0120200049.
- Goldberg, D. E., Melgar, D., Hayes, G. P., Crowell, B. W., and Sahakian, V. J. A ground-motion model for GNSS peak ground displacement. *Bulletin of the Seismological Society of America*, 111 (5):2393–2407, Aug. 2021. doi: 10.1785/0120210042.
- Graves, R. and Pitarka, A. Broadband ground-motion simulation using a hybrid approach. *Bulletin of the Seismological Society of America*, 100(5A):2095–2123, Sept. 2010. doi: 10.1785/0120100057.
- Graves, R. and Pitarka, A. Refinements to the Graves & Pitarka (2010) broadband ground-motion simulation method. *Seismological Research Letters*, 86(1):75–80, 2015. doi: 10.1785/0220140101.
- Hill, E. M., Borrero, J. C., Huang, Z., Qiu, Q., Banerjee, P., Natawidjaja, D. H., Elosegui, P., Fritz, H. M., Suwargadi, B. W., Pranantyo, I. R., Li, L., Macpherson, K. A., Skanavis, V., Synolakis, C. E., and Sieh, K. The 2010 M_W 7.8 Mentawai earthquake: Very shallow source of a rare tsunami earthquake determined from tsunami field survey and near-field GPS data. *Journal of Geophysical Research: Solid Earth*, 117(B6), June 2012. doi: 10.1029/2012jb009159.
- Houston, H. Slow ruptures, roaring tsunamis. *Nature*, 400(6743): 409–410, July 1999. doi: 10.1038/22656.
- Hubbard, J., Barbot, S., Hill, E. M., and Tapponnier, P. Coseismic slip on shallow décollement megathrusts: Implications for seismic and tsunami hazard. *Earth-Science Reviews*, 141:45–55, Feb. 2015. doi: 10.1016/j.earscirev.2014.11.003.
- Ide, S., Imamura, F., and Abe, K. Source characteristics of the Nicaraguan tsunami earthquake of September 2, 1992. *Geophysical Research Letters*, 20(9):836–866, May 1993.
- Jeppson, T. N., Tobin, H. J., and Hashimoto, Y. Laboratory measurements quantifying elastic properties of accretionary wedge sediments: Implications for slip to the trench during the 2011 M_w 9.0 Tohoku-Oki earthquake. *Geosphere*, 14(4):1411–1424, June 2018. doi: 10.1130/ges01630.1.
- Kajiura, K. Tsunami source, energy and the directivity of wave radiation. *Bulletin of the Earthquake Research Institute*, 48:835–869, 1970.
- Kanamori, H. Mechanism of tsunami earthquakes. *Physics of the Earth and Planetary Interiors*, 6(5):346–359, Jan. 1972. doi: 10.1016/0031-9201(72)90058-1.
- Kanamori, H. and Kikuchi, M. The 1992 Nicaragua earthquake: A slow tsunami earthquake associated with subducted sediments. *Nature*, 361(6414):714–716, Feb. 1993. doi: 10.1038/361714a0.
- Kikuchi, M. and Kanamori, H. *Source characteristics of the 1992 Nicaragua tsunami earthquake inferred from teleseismic body waves*, page 441–453. Birkhäuser Basel, Basel, 1995. doi: 10.1007/978-3-0348-7279-9_5.
- Krischer, L. mtspec Python wrappers 0.3.2 [Dataset]. Zenodo, 2016. doi: 10.5281/ZENODO.321789.
- Kuncoro, A. K., Srigutomo, W., and Fauzi, U. Coseismic deformation responses due to geometrical structure and heterogeneity of the accretionary wedge: Study case 2010 Mentawai earthquake, West Sumatra, Indonesia. *International Journal of Geophysics*, 2023:1–13, Jan. 2023. doi: 10.1155/2023/5507264.
- Lay, T. and Bilek, S. 15. *Anomalous earthquake ruptures at shallow depths on subduction zone megathrusts*, page 476–511. Columbia University Press, Dec. 2007. doi: 10.7312/dixo13866-015.
- Lay, T., Ammon, C. J., Kanamori, H., Yamazaki, Y., Cheung, K. F., and Hutko, A. R. The 25 October 2010 Mentawai tsunami earthquake (M_W 7.8) and the tsunami hazard presented by shallow megathrust ruptures. *Geophysical Research Letters*, 38(6), Mar. 2011. doi: 10.1029/2010gl046552.
- Lay, T., Kanamori, H., Ammon, C. J., Koper, K. D., Hutko, A. R., Ye, L., Yue, H., and Rushing, T. M. Depth-varying rupture properties of subduction zone megathrust faults. *Journal of Geophysical Research: Solid Earth*, 117(B4), Apr. 2012. doi: 10.1029/2011jb009133.
- LeVeque, R. J., Waagan, K., González, F. I., Rim, D., and Lin, G. Generating random earthquake events for probabilistic tsunami hazard assessment. *Pure and Applied Geophysics*, 173(12): 3671–3692, Aug. 2016. doi: 10.1007/s00024-016-1357-1.
- Lin, J., Melgar, D., Thomas, A. M., and Searcy, J. Early warning for great earthquakes from characterization of crustal deformation patterns with deep learning. *Journal of Geophysical Research: Solid Earth*, 126(10), Oct. 2021. doi: 10.1029/2021jb022703.
- Lotto, G. C., Dunham, E. M., Jeppson, T. N., and Tobin, H. J. The effect of compliant prisms on subduction zone earthquakes and tsunamis. *Earth and Planetary Science Letters*, 458:213–222, Jan. 2017. doi: 10.1016/j.epsl.2016.10.050.
- Ma, S. and Nie, S. Dynamic wedge failure and along-arc variations of tsunamigenesis in the Japan Trench margin. *Geophysical Research Letters*, 46(15):8782–8790, Aug. 2019. doi: 10.1029/2019gl083148.
- Mai, P. M. and Beroza, G. C. A spatial random field model to characterize complexity in earthquake slip. *Journal of Geophysical Research: Solid Earth*, 107(B11), Nov. 2002. doi: 10.1029/2001jb000588.
- Melgar, D. and Hayes, G. P. Systematic observations of the slip pulse properties of large earthquake ruptures. *Geophysical Research Letters*, 44(19):9691–9698, Oct. 2017. doi: 10.1002/2017gl074916.
- Melgar, D., LeVeque, R. J., Dreger, D. S., and Allen, R. M. Kinematic rupture scenarios and synthetic displacement data: An example application to the Cascadia subduction zone. *Journal of Geophysical Research: Solid Earth*, 121(9):6658–6674, Sept. 2016. doi: 10.1002/2016jb013314.
- Melgar, D., Crowell, B. W., Melbourne, T. I., Szeliga, W., Santillan, M., and Scrivner, C. Noise characteristics of operational real-time high-rate GNSS positions in a large aperture network. *Journal of Geophysical Research: Solid Earth*, 125(7), June 2020. doi: 10.1029/2019jb019197.
- Meng, Q. and Duan, B. Dynamic modeling of interactions between shallow slow-slip events and subduction earthquakes. *Seismological Research Letters*, 94(1):206–216, Oct. 2022. doi: 10.1785/0220220138.
- Meng, Q. and Duan, B. Do upper-plate material properties or fault frictional properties play more important roles in tsunami earthquake characteristics? *Tectonophysics*, 850:229765, Mar. 2023. doi: 10.1016/j.tecto.2023.229765.
- Miyoshi, H. Efficiency of the tsunami. *Journal of the Oceanographical Society of Japan*, 10(1):11–14, 1954. doi: 10.5928/kaiyou1942.10.11.
- Newman, A. V. and Okal, E. A. Teleseismic estimates of radiated seismic energy: The E/M_0 discriminant for tsunami earth-

- quakes. *Journal of Geophysical Research: Solid Earth*, 103(B11): 26885–26898, Nov. 1998. doi: 10.1029/98jb02236.
- Newman, A. V., Hayes, G., Wei, Y., and Convers, J. The 25 October 2010 Mentawai tsunami earthquake, from real-time discriminants, finite-fault rupture, and tsunami excitation. *Geophysical Research Letters*, 38(5), Mar. 2011. doi: 10.1029/2010gl046498.
- Nye, T., Sahakian, V., and Melgar, D. 2010 Mentawai tsunami earthquake simulations [Dataset]. Zenodo, 2024. doi: 10.5281/zenodo.10023345.
- Pedregosa, F., Varoquaux, G., Gramfort, A., Michel, V., Thirion, B., Grisel, O., Blondel, M., Prettenhofer, P., Weiss, R., Dubourg, V., Vanderplas, J., Passos, A., Cournapeau, D., Brucher, M., Perrot, M., and Duchesnay, E. Scikit-learn: Machine learning in Python. *Journal of Machine Learning Research*, 12(85):2825–2830, 2011.
- Prieto, G., Parker, R., and Vernon III, F. A Fortran 90 library for multitaper spectrum analysis. *Computers & Geosciences*, 35(8): 1701–1710, Aug. 2009. doi: 10.1016/j.cageo.2008.06.007.
- Qiu, Q. and Barbot, S. Tsunami excitation in the outer wedge of global subduction zones. *Earth-Science Reviews*, 230:104054, July 2022. doi: 10.1016/j.earscirev.2022.104054.
- Riquelme, S. and Fuentes, M. Tsunami efficiency due to very slow earthquakes. *Seismological Research Letters*, 2021. doi: 10.1785/0220200198.
- Riquelme, S., Schwarze, H., Fuentes, M., and Campos, J. Near-field effects of earthquake rupture velocity into Tsunami Runup Heights. *Journal of Geophysical Research: Solid Earth*, 125(6), June 2020. doi: 10.1029/2019jb018946.
- Ruff, L. J. Do trench sediments affect great earthquake occurrence in subduction zones? *pure and applied geophysics*, 129(1–2): 263–282, Mar. 1989. doi: 10.1007/bf00874629.
- Ruhl, C. J., Melgar, D., Chung, A. I., Grapenthin, R., and Allen, R. M. Quantifying the value of real-time geodetic constraints for earthquake early warning using a global seismic and geodetic data set. *Journal of Geophysical Research: Solid Earth*, 124(4): 3819–3837, Apr. 2019. doi: 10.1029/2018jb016935.
- Ruina, A. Slip instability and state variable friction laws. *Journal of Geophysical Research: Solid Earth*, 88(B12):10359–10370, Dec. 1983. doi: 10.1029/jb088ib12p10359.
- Sahakian, V., Melgar, D., and Muzli, M. Weak near-field behavior of a tsunami earthquake: Toward real-time identification for local warning. *Geophysical Research Letters*, 46(16):9519–9528, Aug. 2019. doi: 10.1029/2019gl083989.
- Sallarès, V. and Ranero, C. R. Upper-plate rigidity determines depth-varying rupture behaviour of megathrust earthquakes. *Nature*, 576(7785):96–101, Nov. 2019. doi: 10.1038/s41586-019-1784-0.
- Sallarès, V., Prada, M., Riquelme, S., Meléndez, A., Calahorrano, A., Grevemeyer, I., and Ranero, C. R. Large slip, long duration, and moderate shaking of the Nicaragua 1992 tsunami earthquake caused by low near-trench rock rigidity. *Science Advances*, 7(32), Aug. 2021. doi: 10.1126/sciadv.abg8659.
- Sandwell, D., Mellors, R., Tong, X., Wei, M., and Wessel, P. Open radar interferometry software for mapping surface deformation. *Eos, Transactions American Geophysical Union*, 92(28): 234–234, July 2011. doi: 10.1029/2011eo280002.
- Satake, K., Bourgeois, J., Abe, K., Abe, K., Tsuji, Y., Imamura, F., Lio, Y., Katao, H., Noguera, E., and Estrada, F. Tsunami field survey of the 1992 Nicaragua earthquake. *Eos, Transactions American Geophysical Union*, 74(13):145–157, Mar. 1993. doi: 10.1029/93eo00271.
- Satake, K., Nishimura, Y., Putra, P. S., Gusman, A. R., Sunendar, H., Fujii, Y., Tanioka, Y., Latief, H., and Yulianto, E. Tsunami source of the 2010 Mentawai, Indonesia earthquake inferred from tsunami field survey and waveform modeling. *Pure and Applied Geophysics*, 170:1567–1582, Sept. 2013. doi: 10.1007/s00024-012-0536-y.
- Scholz, C. H. Earthquakes and friction laws. *Nature*, 391(6662): 37–42, Jan. 1998. doi: 10.1038/34097.
- Small, D. T. and Melgar, D. Can stochastic slip rupture modeling produce realistic M9+ Events? *Journal of Geophysical Research: Solid Earth*, 128(3), Mar. 2023. doi: 10.1029/2022jb025716.
- Tanioka, Y., Ruff, L., and Satake, K. What controls the lateral variation of large earthquake occurrence along the Japan Trench? *Island Arc*, 6(3):261–266, Sept. 1997. doi: 10.1111/j.1440-1738.1997.tb00176.x.
- Tsushima, H. and Ohta, Y. Review on near-field tsunami forecasting from offshore tsunami data and onshore GNSS data for tsunami early warning. *Journal of Disaster Research*, 9(3):339–357, June 2014. doi: 10.20965/jdr.2014.p0339.
- U.S.G.S. Finite fault model maps [Dataset], 2018. <https://earthquake.usgs.gov/earthquakes/eventpage/usp000hnj4/finite-fault>. retrieved July 2023.
- Virtanen, P., Gommers, R., Oliphant, T., Haberland, M., Reddy, T., Cournapeau, D., Burovski, E., Peterson, P., Weckesser, W., Bright, J., van der Walt, S., Brett, M., Wilson, J., Millman, K., Mayorov, N., Nelson, A., Jones, E., Kern, R., Larson, E., Carey, C., Polat, I., Feng, Y., Moore, E., VanderPlas, J., Laxalde, D., Perktold, J., Cimrman, R., Henriksen, I., Quintero, E., Harris, C., Archibald, A., Ribeiro, A., Pedregosa, F., van Mulbregt, P., and SciPy Contributors. SciPy 1.0: Fundamental algorithms for scientific computing in Python. *Nature Methods*, 17(3):261–272, Feb. 2020. doi: 10.1038/s41592-019-0686-2.
- Weinstein, S. and Okal, E. The mantle magnitude M_m and the slowness parameter Θ : Five years of real-time use in the context of tsunami warning. *Bulletin of the Seismological Society of America*, 95(3):779–799, June 2005. doi: 10.1785/0120040112.
- Wessel, P., Luis, J. F., Uieda, L., Scharroo, R., Wobbe, F., Smith, W. H. F., and Tian, D. The Generic Mapping Tools version 6. *Geochemistry, Geophysics, Geosystems*, 20(11):5556–5564, Nov. 2019. doi: 10.1029/2019gc008515.
- Williamson, A. L., Melgar, D., Crowell, B. W., Arcas, D., Melbourne, T. I., Wei, Y., and Kwong, K. Toward near-field tsunami forecasting along the Cascadia Subduction Zone using rapid GNSS source models. *Journal of Geophysical Research: Solid Earth*, 125(8), Aug. 2020. doi: 10.1029/2020jb019636.
- Wirth, E. A., Sahakian, V. J., Wallace, L. M., and Melnick, D. The occurrence and hazards of great subduction zone earthquakes. *Nature Reviews Earth & Environment*, 3(2):125–140, Jan. 2022. doi: 10.1038/s43017-021-00245-w.
- Yao, H., Shearer, P. M., and Gerstoft, P. Compressive sensing of frequency-dependent seismic radiation from subduction zone megathrust ruptures. *Proceedings of the National Academy of Sciences*, 110(12):4512–4517, Mar. 2013. doi: 10.1073/pnas.1212790110.
- Ye, L., Lay, T., Kanamori, H., and Rivera, L. Rupture characteristics of major and great ($M_W \geq 7.0$) megathrust earthquakes from 1990 to 2015: 1. Source parameter scaling relationships. *Journal of Geophysical Research: Solid Earth*, 121(2):826–844, Feb. 2016. doi: 10.1002/2015jb012426.
- Yue, H., Lay, T., Rivera, L., Bai, Y., Yamazaki, Y., Cheung, K. F., Hill, E. M., Sieh, K., Kongko, W., and Muhari, A. Rupture process of the 2010 M_W 7.8 Mentawai tsunami earthquake from joint inversion of near-field hr-GPS and teleseismic body wave recordings constrained by tsunami observations. *Journal of Geophysical Research: Solid Earth*, 119(7):5574–5593, July 2014. doi: 10.1002/2014jb011082.
- Zhang, L., Liao, W., Li, J., and Wang, Q. Estimation of

the 2010 Mentawai tsunami earthquake rupture process from joint inversion of teleseismic and strong ground motion data. *Geodesy and Geodynamics*, 6(3):180–186, May 2015. doi: 10.1016/j.geog.2015.03.005.

Zhao, J., Zhang, J., Asano, A., Ohno, Y., Oouchi, T., Takahashi, T., Ogawa, H., Irikura, K., Thio, H., Somerville, P., Fukushima, Y., and Fukushima, Y. Attenuation relations of strong ground motion in Japan using site classification based on predominant period. *Bulletin of the Seismological Society of America*, 96(3):898–913, June 2006. doi: 10.1785/0120050122.

Zhu, L. and Rivera, L. A. A note on the dynamic and static displacements from a point source in multilayered media. *Geophysical Journal International*, 148(3):619–627, Mar. 2002. doi: 10.1046/j.1365-246x.2002.01610.x.

The article *Modeling ground motions and crustal deformation from tsunami earthquakes: Rupture parameter constraints from the 2010 Mentawai event* © 2024 by Tara A. Nye is licensed under CC BY 4.0.